

https://dspace.org/

The removal of hydroxychloroquine and oseltamivir from wastewater using a simulated labscale biophotocatalytic wastewater treatment plant Activated sludge coupled with calixareneNb2CTxgC3N4 photocatalytic system

Lekgowa Makola; Sharon Moeno; Langelihle Dlamini

https://hdl.handle.net/10539/48252
WOS

Downloaded from a DSpace repository. https://dspace.org/

Chemical Engineering Journal Advances 23 (2025) 100781

Contents lists available at ScienceDirect

Chemical Engineering Journal Advances

journal homepage: www.sciencedirect.com/journal/chemical-engineering-journal-advances

The removal of hydroxychloroquine and oseltamivir from wastewater using a simulated lab-scale bio-photocatalytic wastewater treatment plant: Activated sludge coupled with calixarene@Nb_2CT_x@g-C_3N_4 photocatalytic system

Lekgowa C. Makola [a,b], Sharon Moeno [c], Langelihle N. Dlamini [a,b,*]

[a] Department of Chemical Sciences, University of Johannesburg, P.O. Box 17011, Doornfontein Campus, 2028, Johannesburg, South Africa
[b] Centre for Nanomaterials Science Research, University of Johannesburg, South Africa
[c] Department of Oral Biological Sciences, Faculty of Health Sciences, University of The Witwatersrand, Johannesburg, South Africa

ARTICLE INFO

Keywords:
Hydroxychloroquine
Oseltamivir
Sludge
Photocatalysis
Biodegradation

ABSTRACT

The increasing concerns on water and environmental quality due to the continuous excessive release of antiviral drugs into water systems have received notable attention world-wide. Thus, the development of sustainable environmental remediation technologies is of interest amongst researchers. Herein, a hyphenated bio-photo degradation system was engineered, utilizing activated sludge and a 5-Calixarene@Nb_2CT_x@g-C_3N_4 photocatalytic reactor set-up. The activated sludge was acclimatized to synthetic wastewater for 25 days, reaching COD removal of above 80 %. Mixed liquor suspended solids (MLSSs) and mixed liquor volatile suspended solids (MLVSSs) used to monitor the concentration of suspended solids and the amount of volatile suspended solids reached optimum values of about 2500 mg.L^{-1}, where ideal MLVSSs values of 70–80 % of MLSSs were reached to give MLVSSs/MLSSs ratios of 0.7–0.8. In a 250 mL working solution, the optimum photoreactor parameters were pH 4, 20 mg catalyst loading, and an initial pollutant concentration of 5 mg.L^{-1}. In the hyphenated system, the biodegradation efficiency of 62.5 and 58.1 % for hydroxychloroquine (HCQ) sulphate and oseltamivir (OS) phosphate were obtained, respectively. Photodegradation using 5-CxNbCN increased the removal efficiency to 97.3 and 92.6 % for HCQ and OS, correspondingly. The major contributing reactive oxygen species (ROS) towards the removal of HCQ and OS were e^- and $\bullet O_2^-$ charge carriers. Degradation efficiency was reduced from 80.8 % (control) to 30.7 % in the presence of p-benzoquinone (e^- and $\bullet O_2^-$quencher). Plausible OS and HCQ photodegradation fragments were identified using liquid chromatography mass spectrometry (LC-MS/MS). The parent OS and HCQ ARVs decomposed into smaller organic molecules 3-hydroxycyclohexa-2,5-dien-1-ylium (m/z = 95.05) and 2-aminobenzaldehyde (m/z = 121.05), respectively. This study paves the way towards the realization of practical applicability of solar-powered photocatalysis in conventional WWTPs.

1. Introduction

Frequent global viral pandemics and other emerging infectious diseases (EIDs) including seasonal infections have caused devastating health impact on humans. In recent years, some of the fatal pandemics such as the 1918 Spanish flu (H1N1) and the most recent SARS-CoV-2 (COVID-19) with millions of fatalities have been witnessed [1-3]. These has led to production of large amounts various pharmaceutical drugs such as chloroquine (malaria treatment) and oseltamivir (influenza treatment) as alternatives medicaments to mitigate the severity of the diseases [4,5]. Pharmaceuticals are produce to sustain humans against variety of health complications and infectious diseases. The extensive usage of these pharmaceuticals has led to unprecedented amounts being discharged into the aquatic ecosystems and wastewater treatment plants (WWTPs) [6]. Recent studies reported on the occurrences of COVID-19 treatment-related antiretrovirals (ARVs) and their active metabolites in water sources [7]. Most of WWTPs in developing countries such as South Africa are ineffective towards the removal of these ARVs and their metabolites in wastewater [8]. A study by Abafe and colleagues reported on the detection of high concentrations of ARVs

* Corresponding author.
E-mail address: lndlamini@uj.ac.za (L.N. Dlamini).

https://doi.org/10.1016/j.ceja.2025.100781

Available online 26 May 2025
2666-8211/© 2025 The Author(s). Published by Elsevier B.V. This is an open access article under the CC BY license (http://creativecommons.org/licenses/by/4.0/).

in influents and effluents of WWTPs in KwaZulu-Nata, South Africa [9].

Pharmaceuticals including ARVs are amongst some of the most environmentally persistent pollutants which disseminate into the aquatic milieu and WWTPs [7]. The use of the ineffective conventional water treatment methods in WWTPs leads to the ubiquitous and constant occurrences of these pharmaceuticals in treated water. Conventional WWTPs mainly utilizes activated sludge system to facilitate biological degradation of various pollutants including pharmaceuticals from wastewater. However, most of these pharmaceuticals are highly soluble and resistant to biodegradation, rendering the activated sludge technique inefficient. Failure to remove the ARVs from the WWTPs could consequently end up in the aquatic environments and drinking water [10]. Persistence pollutants such as chloroquine and oseltamivir in the environment poses an ecological health risk to human and animal through the risk of developing multidrug-resistant infections [6,10]. Hence it is essential to design effective techniques for the complete removal of these antiviral drugs from wastewater.

Commonly used wastewater treatment techniques include chemical treatments, adsorption, advanced oxidation processes, membrane filtration, and biodegradation [11-13]. Advanced oxidation processes (AOPs), state-of-the-art water purification techniques, have acquired immense interest worldwide towards the elimination of these pollutants of emerging concern (PECs). Within the class of AOPs, photocatalysis is identified as the most propitious treatment technique, accounting for extensively stable and reusable photocatalysts with the ability to facilitate complete pollutants mineralization into CO_2 and H_2O [11]. Furthermore, photocatalytic processes can be initiated by irradiating the surface of photocatalysts with the abundant solar energy (342 $J.s^{-1}$ per m^2 hitting the surface of Earth yearly) [14]. As a result, photocatalysis is rendered ideal for sustainable development as it operates under ambient conditions.

An adequate number of photocatalysts with merit properties have been explored towards the removal of pharmaceutical compounds (PCs) in aqueous media, to name a few; Nb_2O_5-RGO/MoO_3 (sulfasalazine (Azulfidine) and ciprofloxacin) [15], g-C_3N_4/Nb_2O_5, $ZnWO_4$/Bi_2MoO_6, and $FeIn_2S_4$/BiOBr (tetracycline) [16-18], g-C_3N_4 (carbamazepine) [19], and l-BP@Nb_2O_5 (nevirapine) [20]. Nevertheless, the removal of ARVs from real wastewater samples using photocatalysis has rarely been explored. Recently, a study by Rapti *et al.* reported on the photodegradation of pharmaceuticals from real hospital wastewater, where carbamazepine, amisulpride, O-desmethyl venlafaxine, and venlafaxine were detected in all the aliquot samples [19]. Concentrations of about 2.924 μg L^{-1} for O-desmethyl venlafaxine and 0.073 μg L^{-1} for citalopram were detected [19]. Using g-C_3N_4 under solar irradiation in a lab-scale reactor, up to 96 % and 34 % of amisulpride and mirtazapine were removed, respectively [19]. In addition, Evgenidou et al. reported on a complete degradation of antiviral drug abacavir in ultrapure water [21]. Lele et al. also reported on the removal of oseltamivir in a simulated wastewater treatment plant (WWTP) using WO_3-Ti_3C_2@β-CD with up to 93 % degradation efficiency [12]. A recent study by Gayathri and colleagues demonstrated the photodegradation of chloroquine in water using ZnO under solar and ultraviolet (UV) irradiation, where 77 % and 65 % removal efficiencies were observed for solar and UV irradiation, respectively [22]. The above-discussed studies demonstrate promising results toward advancing this cutting-edge technology for complete mineralization of ARVs in water.

For a more realistic evaluation of the removal of the dissolved pharmaceuticals including ARVs from water, it is imperative to conduct studies in real wastewater samples to validate practical feasibility of photocatalysis. Thus, the present study focuses on the removal of chloroquine and oseltamivir from synthetic wastewater. Additionally, a lab-scale WWTP was engineered to mimic a biological treatment unit in a conventional wastewater treatment plant used in South African wastewater treatment systems. Activated sludge and domestic real wastewater were obtained from a conventional WWTP to inoculate the lab-scale WWTP. The configuration and acclimatization processes in the WWTP were adopted from the OECD 303A guideline and from our previous studies [23-25]. Activated sludge is brown in colour, consisting of a cocktail of microorganisms of which 95 % comprises aerobic bacteria cultured in aeration tanks and are capable of decomposing organic matter in aqueous media [26]. In most cases, well-operated activated sludge (carrying mixed liquor suspended solids - MLSS between 2000 and 5000 mg/L) provides reasonable removals (85–95 %) of biochemical oxygen demand (BOD_5, <30 mg/L), chemical oxygen demand (COD, >70 %), and other biodegradable organics [26,27]. The lab-scale activated sludge system is hyphenated to a photocatalytic system to incorporate photodegradation as a tertiary water treatment process.

Photocatalysis has the potential to facilitate the mineralization of non-biodegradable pollutants such as ARVs from wastewater. Photocatalysts used herein were fabricated from non-noble metal and eco-friendly semiconductor and organic materials. The use of organic-based semiconductor materials without noble metals helps to reduce the overall cost of photocatalyst fabrication. Additionally, only minimal amounts of transition metal-based co-catalysts were employed to enhance the photocatalyst's activity. The photocatalytic process involves aqueous phase degradation of pollutants through highly reactive oxygen species (ROS) namely, superoxide (O_2•-), hydroxyl radical (•OH), hydrogen peroxide (H_2O_2), and singlet oxygen ($^1O_2$) [22]. The design of metal-free, eco-friendly, cost-effective, and visible-light highly responsive photocatalysts has gained considerable attention among researchers. Graphitic carbon nitride (g-C_3N_4) is amongst the extensively studied semiconductor materials, owing to its environmentally friendly nature, excellent chemical stability, layered structure, narrow energy bandgap, and suitable band positions [28]. Just like many other single semiconductor materials, g-C_3N_4 photocatalytic performance is limited by the inefficient visible light absorption ability and rapid relaxation of photoexcited charge carriers [29,30]. In our previous study, it was demonstrated that the formation of heterostructures enhanced the optical and photoelectrochemical properties of g-C_3N_4 [31]. The heterostructure formation was achieved by introducing a highly conductive two-dimensional (2D) material known as MXene onto g-C_3N_4 (CN) nanosheets. Particularly, niobium carbide Nb_2CT_x (Nb) MXene was used to form the Nb_2CT_x@g-C_3N_4 (NbCN) Schottky-junction. In another study, Nb_2CT_x@g-C_3N_4 was further functionalized with a supramolecule in the form of calixarene (calix[4]arene) complex to induce sensitizations in the photocatalyst [32]. Briefly, the three-component calixarene-based composite Calix@Nb_2CT_x@g-C_3N_4 (CxNbCN) was rationally designed to maximize the photocatalytic efficiency of the Nb_2CT_x@g-C_3N_4 Schottky-junction. Calixarene complexes in the heterostructure facilitated sensitization and consequently improved light absorption ability [32].

In the present study, the efficiency of a photocatalytic system hyphenated to activated sludge simulated WWTP was evaluated towards the degradation of hydroxychloroquine (HCQ) and oseltamivir (OS) ARVs pollutants in wastewater. The activated sludge contains microorganisms which induces biodegradation processes in the system [26]. The photocatalytic system was equipped with a three-component photocatalyst (Calix@Nb_2CT_x@g-C_3N_4) for the effective decomposition of the pollutants. In the photocatalytic system, the degradation efficiency of Calix-Nb_2CT_x@g-C_3N_4 was significantly high compared to Nb_2CT_x@g-C_3N_4 due to the presence of calixarene complexes which induces synchronous host-guest interaction with the pollutants and photocatalytic sensitization effect. Furthermore, the bio-photocatalytic wastewater treatment system used in this study lays out a pathway toward the incorporation of visible-light-driven photocatalysis in conventional WWTP for the removal of antiviral drugs in different water metrices.

2. Experimental

Analytical instruments descriptions and operating conditions are detailed in the supplementary information (SI).

2.1. Materials and reagents

Chemicals and reagents used as received, unless stated in the discussion. The antiviral drugs hydroxychloroquine sulphate (≥98 %) and oseltamivir phosphate (≥98 %) were obtained from Sigma-Aldrich South Africa. Reagents for photon flow measurements; iron(III) sulfate hydrate ($Fe_2(SO_4)_3.xH_2O$, ≥97 %), Iron(II) sulfate heptahydrate ($FeSO_4{\cdot}7H_2O$, ≥98 %), 1,10-phenanthroline (≥99 %), oxalic acid (anhydrous, ≥99.0 %), sodium acetate (ACS reagent, ≥99.0 %), sulphuric acid (ACS reagent, 98.0 %) were also acquired from Sigma-Aldrich South Africa. Meat extract dry (for microbiology), di-potassium hydrogen phosphate (anhydrous, ≥99.99 %), magnesium sulphate heptahydrate (ACS reagent, ≥99.0 %), peptone from meat extract (bacteriological), urea crystals (ACS reagent, ≥99.0 %), calcium chloride dehydrate ReagentPlus®, ≥97.0 %), and sodium chloride (ACS reagent, ≥99.0 %) used in the WWTP were obtained from Merck and Sigma-Aldrich South Africa. Radical trapping experiments reagents; p-benzoquinone (reagent grade, ≥98.0 %), ethylenediaminetetraacetic acid (ACS reagents, ≥99.4 %), potassium dichromate (ACS reagent, ≥99.0 %), and 2-propanol (ACS reagent, ≥99.5 %) were also purchased from Sigma-Aldrich South Africa.

2.2. Photocatalysts

In this work, Schottky-junction photocatalysts composed of graphitic carbon nitride (g-C_3N_4), niobium carbide MXene (Nb_2CTx), and calixarene (calix[4]arene-25,26,27,28-tetrol) were employed towards the degradation of hydroxychloroquine (HCQ) and oseltamivir (OS). The detailed material characterizations, optoelectronic, and photoelectrochemical properties of the pristine and the photocatalytic nanocomposites were reported in our previous studies [31,32]. Briefly, the photocatalysts used herein were all derived from g-C_3N_4 used as a primary photocatalyst. Initially, g-C_3N_4 was integrated into Nb_2CTx MXene to form the g-C_3N_4@Nb_2CTx Schottky-junction, followed by covalent linkage with an acyl chloride functionalized calix[4]arene-25,26,27,28-tetrol to form a calixarene sensitized Schottky-junction (presented as Calix@g-C_3N_4@Nb_2CTx). The abridged name "Calix" in the composite name represents the introduced calix[4]arene-25,26,27,28-tetrol complex. The prepared photocatalysts from our previous studies were as follows; pristine g-C_3N_4, g-C_3N_4 modified with 1,3, and 5 wt percentages (wt %) of Nb_2CT_x MXene (forming Y-Nb_2CT_x@g-C_3N_4, where Y is wt % of MXene), g-C_3N_4 modified with 10wt % of calixarene, and lastly Y-Nb_2CT_x@g-C_3N_4 composites modified with 10wt % of calixarene (forming Y-Calix@Nb_2CT_x@g-C_3N_4). The as-prepared 5-Calix@Nb_2CT_x@g-C_3N_4 ternary nanocomposite exhibited enhanced visible light response with a narrowed energy bandgap (E_g) of 1.79 eV relative to the pristine g-C_3N_4 with E_g of 2.62 eV [32]. Furthermore, excellent photoelectrochemical properties were observed for the 5-Calix@Nb_2CT_x@g-C_3N_4 ternary composite, with a corresponding photo-to-chemical conversion efficiency (η) of 2.42 % [32]. The photocatalytic energy band diagram delineated suitable band positions for 5-Calix@Nb_2CT_x@g-C_3N_4 towards the generation of reactive oxygen species (ROS) necessary for pollutants degradation. The oxidizing valence band (VB) and the reducing conduction band (CB) potential for 5-Calix@Nb_2CT_x@g-C_3N_4 were 1.65 and −0.14 V vs. NHE, respectively. Table 1 presents the photocatalysts employed in this work towards the photodegradation of HCQ and OS. The composite 5-Calix@Nb_2CT_x@g-C_3N_4 was chosen for this study owing to its superior optical and photoelectrochemical properties over the 1-Calix@Nb_2CT_x@g-C_3N_4 and 3-Calix@Nb_2CT_x@g-C_3N_4 composites [32].

Table 1
Photocatalysts descriptions and weight percentage compositions.

Photocatalyst	Abridged name	Composition (wt %)		
		g-C_3N_4	Nb_2CT_x	Calixarene
g-C_3N_4	CN	100 wt %	–	–
5-Nb_2CT_x@g-C_3N_4	5-NbCN	95 wt %	5 wt %	–
Calixarene@g-C_3N_4	CxCN	90 wt %	–	10 wt %
5-Calixarene@Nb_2CT_x@g-C_3N_4	5-CxNbCN	85 wt %	5 wt %	10 wt %

(-) No value.

2.3. Wastewater treatment plant configuration

2.3.1. Activated sludge system

A lab-scale wastewater treatment plant (WWTP) was assembled to mimic a conventional wastewater treatment plant (WWTP). The set-up consists of four major components; (i) influent holding tank (feeding the plant, 20 L), (ii) aeration tank (aerobic biodigestion, 3 L), (iii) circular settling tank (clarifier, 1.5 L), and (iv) the effluent holding tank (bio-treated, 20 L) which works concurrently to purify wastewater (see Fig. 1). The treatment system was assembled in a continuous stirred-tank bio-reactor configuration as shown in Fig. 1. The digital images of the exact lab-scale simulated WWTP are presented in **Fig. S1**. The operation of the lab-scale WWTP herein is per the OECD 303A of aerobic-activated sludge treatment [23]. Typically, wastewater (domestic effluent) is fed into the system through peristaltic pump from the influent storage tank, where it flows into the aeration tank for microbial digestion of various organic pollutants. Aerobically biodegraded contaminants are precipitated out of the wastewater and allowed to settle in the clarifier tank. Lastly, biologically treated water flows into the holding tank for further tertiary treatment processes shown in Fig. 1. The wastewater is filtered before being fed to the system (as influent) to avoid solid materials from clogging up the flow channels. Detailed descriptions of the apparatus used in the assembly of the lab-scale WWTP are outlined in the **SI**.

2.3.2. Wastewater and activated sludge sampling and inoculation

Activated sludge for the inoculation of the lab-scale WWTP was acquired from a conventional WWTP in Daspoort (Pretoria), South Africa. The sludge was sampled from the agitation/aeration step, where it is already fed with wastewater. Influent entering the Daspoort WWTP was also sampled to mimic the operating conditions in the lab-scale WWTP for ease of acclimatization processes. The samples were stored at 4 °C in a refrigerator and retained for a maximum of 7 days. Sampling was conducted weekly during the acclimatization process to maintain a continuous operation of the laboratory lab-scale WWTP. After the activated sludge was inoculated into the lab-scale WWTP, the sampled wastewater was fed to the system and allowed to circulate through the treatment system. During the inoculation, activated sludge was aerated for 6 h and introduced into the aeration tank, followed by feeding with a mixture of wastewater and supernatant resulting from aeration of the sludge. The wastewater was gradually mixed with synthetic wastewater (SWW) for over 20 days until 100 % of SWW was used as influent. Wastewater was retained in the system for an average of 6 h (known as hydraulic retention time, HRT) at a constant effluent flow rate of 0.5 $L.h^{-1}$. The activated sludge was retained in the system for 5 days, referred to as sludge retention time (SRT). A portion of circulating sludge (0.6 L/day) was discarded as waste-activated sludge (WAS) and the return-activated sludge (RAS) was re-circulated back into the aeration tank as shown in Fig. 1. The was used to conduct tests to monitor the sludge bioactivity. The lab-scale WWTP delineated by the schematic illustrations in Fig. 1 imitates real conventional WWTP, thus operating under controlled conditions.

2.3.3. Acclimatization: critical parameters

It is necessary to reach optimal working conditions in the lab-scale WWTP to maximize removal efficiency of pollutants from wastewater. Hence, several parameters are sequentially evaluated to monitor the

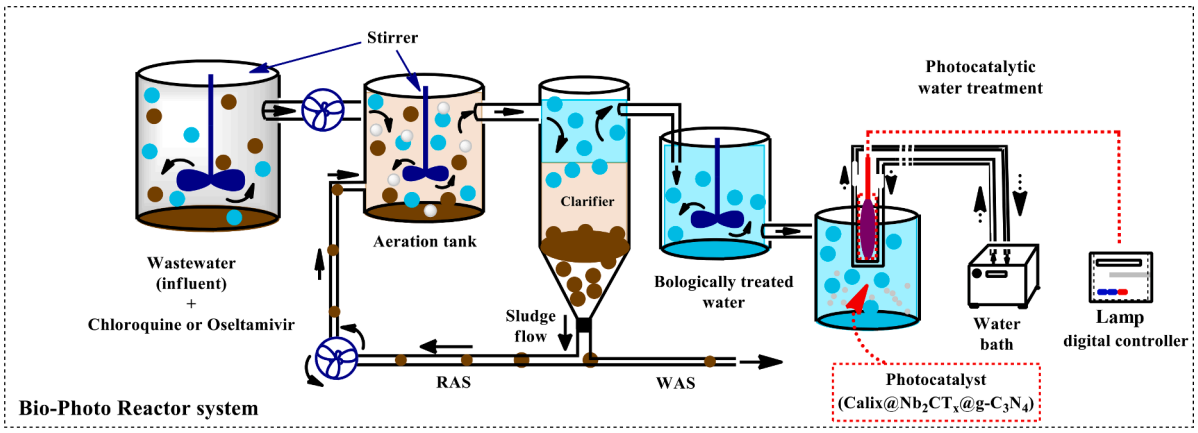


Fig. 1. Schematic illustration of a hyphenated activated sludge and photocatalytic reactor lab-scale wastewater treatment plant.

condition of the activated sludge and the treated water. In the first 3 to 5 days of inoculation (SRT 1), the system was fed with pre-treated supernatant from the sludge and wastewater to acclimatize the activated sludge to the new environment. The system was continuously operated for 25 days (SRT 5) to reach a steady state (optimal operation) thereafter used to biodegrade HCQ and OS from the SWW. The SWW was formulated in deionized water according to **Table S1** (**SI**) and the ratios of domestic wastewater to the SWW over time from SRT 1 to SRT 5 are shown in **Table S2** (**SI**). Synthetic wastewater was used to feed the microorganisms (sludge) and to control the effluent chemical compositions by introducing only known chemical reagents. During the acclimatization, the temperature of the system was maintained at 20–25 °C using aeration and settling tanks equipped with continuously circulating water. Compressed air (2 mg.L^{-1}) was bubbled into the aeration chamber to facilitate aerobic conditions for microbial growth.

Critical parameters were monitored including analytical tests such as chemical oxygen demand (COD), pH, conductivity, dissolved oxygen (DO), mixed liquor suspended solids (MLSSs), mixed liquor volatile suspended solids (MLVSSs), and the activated sludge volume index (SVI) were studied similarly to our previous reports [24,25,33]. Parameters such as pH, DO, and conductivity were evaluated to assess the system operating conditions, whilst MLSSs, MLVSSs, and SVI were used to evaluate the bio-activity and colloidal behaviour of the activated sludge. The pH was maintained at 7 using dilute (0.01 M) solutions of NaOH and HCl. The conversion of the organic pollutants was assessed by conducting COD cell test (Sigma-Aldrich, SQ COD CT 25–1500 mg/L) on a spectrophotometer. The COD was conducted routinely for both the influent and the effluent. Aliquots used for COD measurements were filtered prior digestion using 0.45 μm polyvinylidene fluoride (PVDF) syringe filter disks. For MLSSs and MLVSSs evaluations, 100 mL of the activated sludge was sampled from the aeration chamber and filtered through Whatman glass microfiber filter (Sigma-Aldrich, WHA1820090). The sludge was dried at 105 °C for 12 h for MLSSs calculations (using **Eq. S1** (**SI**)) and further calcined at 550 °C for 15 min to calculate the MLVSSs (using **Eq. S2** (**SI**)). Furthermore, 500 mL of the was used for SVI evaluations, where it was placed in a 1000 mL graduated measuring cylinder and filled with water. The sample was allowed to settle for 30 min and the volume of settled sludge was recorded and the SVI was calculated according to **Eq. S3** (**SI**). All the measurements in the treatment plant were conducted daily.

2.3.4. *Hyphenated activated sludge and photocatalytic reactor*

Tertiary water treatment process in the form of a photocatalytic reactor was hyphenated to the conventional lab-scale WWTP as a post treatment as delineated in Fig. 1 and digital images in **Fig. S1**. The photocatalytic reactor in the hyphenated wastewater treatment system was directly connected to the holding tank of the biologically pre-treated water in the form of a continuous system (see Fig. 1). The biologically pre-treated wastewater from the effluent holding tank was transferred to a Lelesil photochemical reactor system (Lelesil Innovation System, India) for further treatment with photocatalysis as a tertiary water treatment technique. The light source used in the photochemical reactor was either a 250 W high-pressure visible light or a 250 W high-pressure Mercury Ultraviolet (UV) (250–450 nm) lamp powered by a 230 V AC power source. The reactor was equipped with a borosilicate glass layer connected to a water-cooling unit to reduce the thermal energy produced by the light source. The photoreactor was employed to photodegrade the biodegradation resistant hydroxychloroquine sulfate (HCQ) and oseltamivir phosphate (OS) post-activated sludge treatment. Briefly, 500 mL of the effluent from the activated sludge system was transferred to a photoreactor. A known concentration of photocatalysts was then introduced to the sample and stirred in the dark for 30 min before being irradiated with either UV or visible light. The concentration of the pollutant was assessed at three stages in the treatment process, (i) influent holding tank activated sludge system, (ii) effluent holding tank of activated sludge system, and (iii) after being treated in the photoreactor.

2.4. *Photonic flux measurements*

Photon flux studies were conducted to evaluate the irradiation intensities of the light sources used in the photocatalytic reactor. The influence of photon energy (λ, wavelength) on the photon flux (light intensity) was evaluated by comparing the incident photon flow (I_0) of a 250 W visible light to a 250 W UV light powered by the 230 V AC lamp controller. The photon flow experiments were conducted using an actinometric solution (potassium ferrioxalate, Fe^{3+}) and using calorimetric analysis for quantification following a procedure by Hatchard and colleagues [34]. Briefly, 500 mL of actinometric solution containing ferric sulphate (1.47 g.L^{-1}, 0.003 M), oxalic acid (2.269 g.L^{-1}, 0.018 M), and 100 mL of sulphuric acid (1 N, 0.5 M) was prepared and irradiated with either ultraviolet (UV) or visible light sources. The solution was irradiated for 10 min with 2 min intervals of 2 mL aliquot sampling. The samples were quantified using calorimetric solution following the procedure detailed on the supplementary information (**SI**). The Fe^{2+} standard calibration curve was deduced using **Table S4** (**SI**).

2.5. *Photodegradation optimization parameters*

Optimum operating conditions for the photodegradation of HCQ and OS were evaluated in a 250 mL photoreactor system. Three fundamental parameters were sequentially evaluated, (i) solution working pH, (ii) pollutant concentration (in mg.L^{-1}), and lastly (iii) photocatalyst loading (in mg). Various factors such as the photocatalyst surface charge and

functional groups are affected by these variables, where pH could have an impact on the interactions between the photocatalyst and pollutant [35]. A detailed experimental method for the optimization of these parameters is outlined in the supplementary information (**SI**). Generally, pharmaceuticals retain their molecular form when the solution pH is less than the pKa, and forms a conjugate base when pH is larger than the pKa [36]. The change in surface charges could have an impact on the photocatalytic activities, owing to the presence or absence of electrostatic interactions between the pollutant and the photocatalyst [37]. Thus, the effect of pH on the zeta potential (surface charge, ζ) for both the pollutants and the photocatalysts were evaluated in different pH conditions from acidic (pH 1) to basic (pH 13). Photodegradation studies were also conducted at different pH values from 1 to 13 for all the materials, to ascertain the influence of pH on the activity of the materials. Furthermore, photocatalysts concentrations were optimized, ranging from 5 to 20 mg at constant increments of 5 mg. The pollutants concentrations were also optimized from 5 to 25 $mg.L^{-1}$ with a constant increment of 5 $mg.L^{-1}$. All the photocatalytic degradation studies were conducted using a working volume of 250 mL. The photocatalytic measurements were conducted in triplicated to maintain consistency and reliability of the data.

2.6. Degradation and quantification methods

Preliminary evaluations for the removal of hydroxychloroquine sulfate and oseltamivir phosphate from wastewater were conducted using COD and ultraviolet-visible (UV–Vis) spectrophotometer. The percentage COD removals (% COD removal) were evaluated during acclimatization and during the treatment of the drugs in the activated sludge system. The % COD removals were relatively calculated using Eq. (1) [24].

$$\%COD\ Removal = \frac{(C_i - C_f)}{C_i} \times 100 \quad (1)$$

Where C_i (ppm) and C_f (ppm) are the initial (influent) and final (effluent) concentrations in the treatment system, respectively. UV–Vis spectrophotometer calibration standards were obtained based on the concentrations 1, 5, 10, 15, 20, and 25 ppm. After irradiation at different time intervals, aliquots were filtered through 0.45 μm polyvinylidene fluoride (PVDF) syringe filter disks to remove suspended photocatalytic materials. The UV–Vis absorption for HCQ was recoded at λ_{max} = 343 nm and for OS was recorded at λ_{max} = 218 nm absorption bands. The obtained concentrations were used to determine the removal efficiencies following Eq. (2) [24,38].

$$\%\ Drug\ Removal = \frac{(C_0 - C_t)}{C_t} \times 100 \quad (2)$$

Where C_0 and C_t are the concentration (ppm) at time = 0 min and time = t min, correspondingly. The photodegradation kinetics were studied through Eq. (3) reported elsewhere [24].

$$-\ln\left(\frac{C_0}{C_t}\right) = kt \quad (3)$$

Where C_0 and C_t are the concentration at time = 0 min and time = t min, k is the degradation rate constant (min^{-1}). The rate constants were evaluated to demonstrate the acceleration or deceleration of pollutants degradation rates under different parameters/variables.

To further ascertain for the bio- and photo-degradation processes observed using COD and UV–Vis spectrophotometer, respectively, liquid chromatography mass spectrometry (LC-MS/MS) was employed for a comprehensive analysis of the degradation products and consequently derive of HCQ and OS degradation pathways.

3. Results and discussion

3.1. Photocatalysts characterizations

Comprehensive discussions on the syntheses and characterizations of the photocatalysts employed in this study can be accessed by referring to our previous works [31,32]. In summary, bare g-C_3N_4, Nb_2CT_x MXene, and the Schottky-junction between Nb_2CT_x and g-C_3N_4 were reported initially, followed by the formation of a three-component photocatalyst between g-C_3N_4, Nb_2CT_x, and calix[4]arene-25–26–27–28-tetra-OCH_2COCl supramolecular cyclic oligomer. Fig. 2**(a)** shows scanning electron microscopy (SEM) images and energy dispersive X-ray spectroscopy (EDX-S) spectra of the three component photocatalyst 5-CxNbCN. Combination of g-C_3N_4 irregular morphology and Nb_2CT_x nanosheets were observed for the 5-CxNbCN composite. The corresponding expected elemental compositions for 5-CxNbCN were observed on the EDS-X spectra (see Fig. 2**(a)**). Elemental mapping also demonstrated a uniform distribution of the materials in the composite (**Fig. S6**). Transmission electron microscopy (TEM) was further employed to study the morphology of the as-fabricated photocatalysts. The nanocomposite 5-NbCN presents a layered structural morphology attributed to the presence of both Nb_2CT_x MXene and g-C_3N_4, with respect to the pristine g-C_3N_4 shown in Fig. 2**(b)**. The introduction of calixarene onto the g-C_3N_4 was validated by the formation of porous g-C_3N_4 (CN) morphology. Crystal structures of the photocatalysts were evaluated using XRD (Fig. 2**(c)**). Moreover, CN exhibits two typical peaks indexed to (100) and (002), ascribed to the g-C_3N_4 aromatic heterocycles and the triazine fragments, respectively [31]. The composites 5-NbCN and 5-CxNbCN both presented XRD peaks from CN and the Nb_2CT_x MXene, denoted by diamonds and hearts, respectively (see **Fig. 2(c)**). The XRD characteristic peaks of the calix[4]arene-25,26,27,28-tetrol complex were not distinctly observed in the spectra of the composites due to the low loading contents (10 wt %) and the amorphous nature of the calixarene complexes [32]. The amorphous nature of the acyl chloride functionalized calix[4]arene-25,26,27,28-tetrol complex was evidenced by the XRD analysis in our preceding work [32]. The XPS survey scan further confirmed the presence of all the expected elements in all the pristine photocatalysts and the composites (See Fig. 2**(d)**). Comprehensive discussions on the high-resolution XPS analysis were reported in our previous studies [31,32].

Optical and photoelectrochemical techniques were employed to study photon absorption and charge transfer kinetics of the photocatalysts. Tauc plots in Fig. 3**(a)** present a narrowed energy band gap for the ternary composite 5-CxNbCN (E_g = 1.79 eV) relative to the dual composites 5-NbCN (E_g = 2.16 eV) and Cx-CN (E_g = 2.23 eV) and the pristine CN (E_g = 2.62 eV), signifying enhanced photon absorption ability upon the formation of the composites. The photoluminescence (PL) spectra in Fig. 3**(b)** showed significantly low intensity for 5-CxNbCN photocatalyst relative to the pristine CN, suggesting reduced charge recombination rates upon the heterostructure formations. The Schottky-junction photocatalyst 5-NbCN exhibited low PL intensity compared to the CxCN, owing to the lower Fermi level of MXene acting as an electron sink to restrain recombination of photoexcited charge carriers. The charge transfer kinetics were evaluated using Nyquist plots in Fig. 3**(c)**. Randles-Ershler equivalent circuit model was used for the determination of the charge transfer resistance [32]. Based on the Nyquist curves in Fig. 3**(c)**, 5-NbCN presented a smaller semi cycle, suggesting the least charge transfer resistance relative to 5-CxNbCN. This is owing to the excellent Nb_2CT_x MXene charge transfer abilities compared to the introduced calixarene (calix[4]arene-25,26,27,28-tetrol) complex in 5-CxNbCN. The photocurrent response plots in Fig. 3**(d)**, further confirm excellent photoinduced charge carrier separations for the 5-CxNbCN composites followed by 5-NbCN and CxCN. Detailed optoelectronic and photoelectrochemical parameters were comprehensively discussed in our previous works on the synthesis and characterization of the reported materials [31,32].

Mott-Schottky (MS) plots presented in Fig. 4 **(a-d)** obtained using an

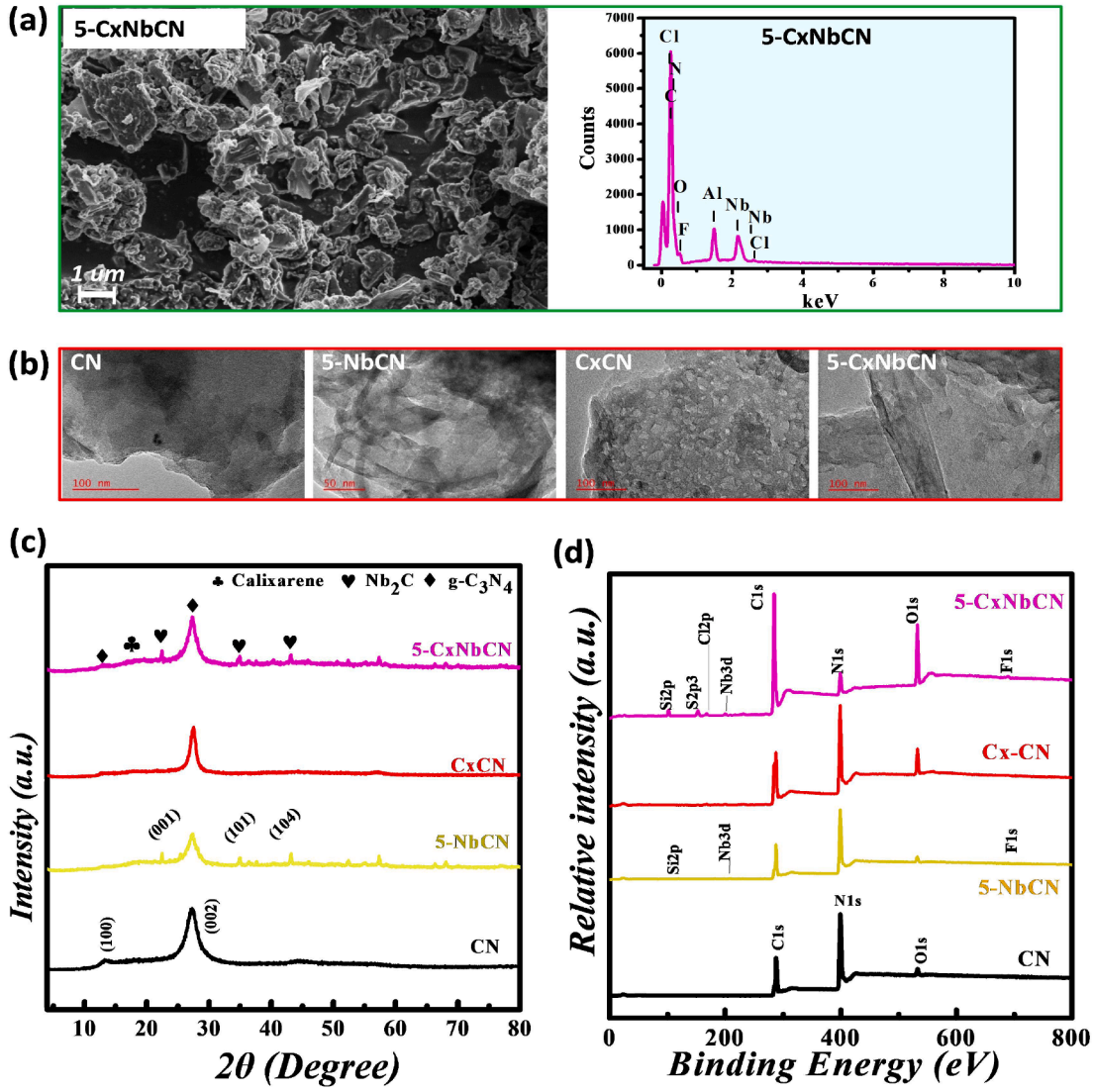


Fig. 2. SEM and EDS analysis of 5-CxNbCN (a), TEM images of CN, 5-NbCN, CxCN, and 5-CxNbCN (b), XRD spectra (c), and XPS survey spectra (d) of CN, 5-NbCN, CxCN, and 5-CxNbCN [31,32].

electrochemical workstation were used to construct photocatalytic band diagrams from the photocatalysts flat band potentials (V_{fb}), and consequently evaluate the redox potential abilities. Furthermore, the positive linear gradient for all the MS plots suggests the formations of n-type semiconductors [39]. The V_{fb} of the photocatalysts were extrapolated to be −1.05, −0.09, −0.65, −0.24 (V vs. Ag/AgCl) for CN, 5-NbCN, CxCN, and 5-CxNbCN, respectively (See Fig. 4 **(a-d)** and Table 2). From the V_{fb} values, the conduction band potentials V_{CB} were derived to be −0.95, +0.01, −0.55, and −0.14 (V vs. NHE), for CN, 5-NbCN, CxCN, and 5-CxNbCN, subsequently [40]. Photocatalyst carrier concentration (donor, N_D) calculations were detailed and discussed in our previous works [31,32]. Fig. 4**(e)** presents photocatalytic band potential diagrams, were the redox band potentials are observed to slightly shift upon the formation of the heterojunctions. Notable positive (to the oxidizing side) shifts in the band potentials were observed upon the formation of the Schottky-junction 5-NbCN followed by 5-CxNbCN. This phenomenon signifies the superior co-catalyst effect brought by Nb_2CT_x MXene on the intrinsic electronic structure of the CN. Furthermore, excellent valence band potential (V_{VB}) of +2.17 V for 5-NbCN suggests an ability to facilitate oxidation reactions. The calixarene-sensitized Schottky--junction 5-CxNbCN presents a narrow E_g and band potentials with redox potencies capable of facilitating both reduction and oxidation reactions.

3.2. *Lab-scale wastewater treatment plant: operation and acclimatization*

The primary focus of this work was to develop an efficient hyphenated bio-photocatalytic wastewater treatment process by employing an activated sludge system and semiconductor-based photocatalysis. This hyphenated bio-photocatalytic system was utilized towards the removal of HCQ and OS from wastewater. In an effort to maximize the efficiency of the wastewater treatment process, the activated sludge system (biodegradation unit) was acclimatized to synthetic wastewater (SWW) and the new environment in the lab-scale wastewater treatment plant (PSWWTP). Several parameters were evaluated over a period of 25 days, during which the activated sludge was acclimatized to the SWW and reached system steady state. Mixed liquor suspended solids (MLSSs) and mixed liquor volatile suspended solids (MLVSSs) were used to evaluate the concentration of suspended solids and the amount of volatile suspended solids in the activated sludge agitation unit, respectively [41]. The parameter MLSSs assesses the organic, inorganic, volatile, and non-volatile solids whilst the parameter for MLVSSs is used to monitor only the volatile organic or biomass in the system. In the initial stages of the acclimatization process (SRT 1), both the MLSSs and MLVSSs values were significantly low, and continued to decrease to 645 $mg.L^{-1}$ on the third day of inoculation (See Fig. 5**(a)**). This drastic fall in both the

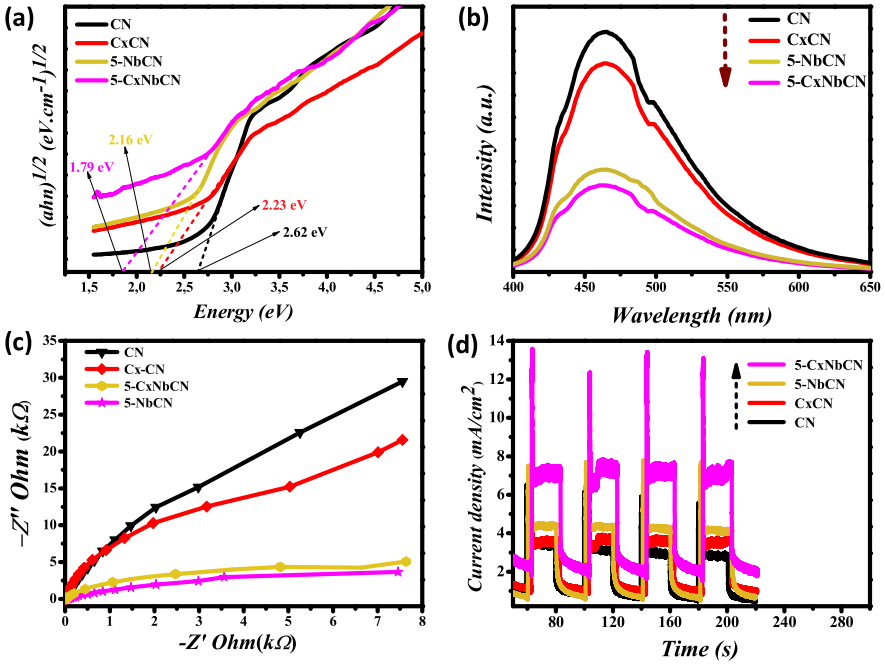


Fig. 3. UV–Vis DRS derived Tauc plots (a), steady state photoluminescence spectra (b), electrochemical Nyquist plots (c), and electrochemical photocurrent response spectra (d) for the photocatalysts [31,32].

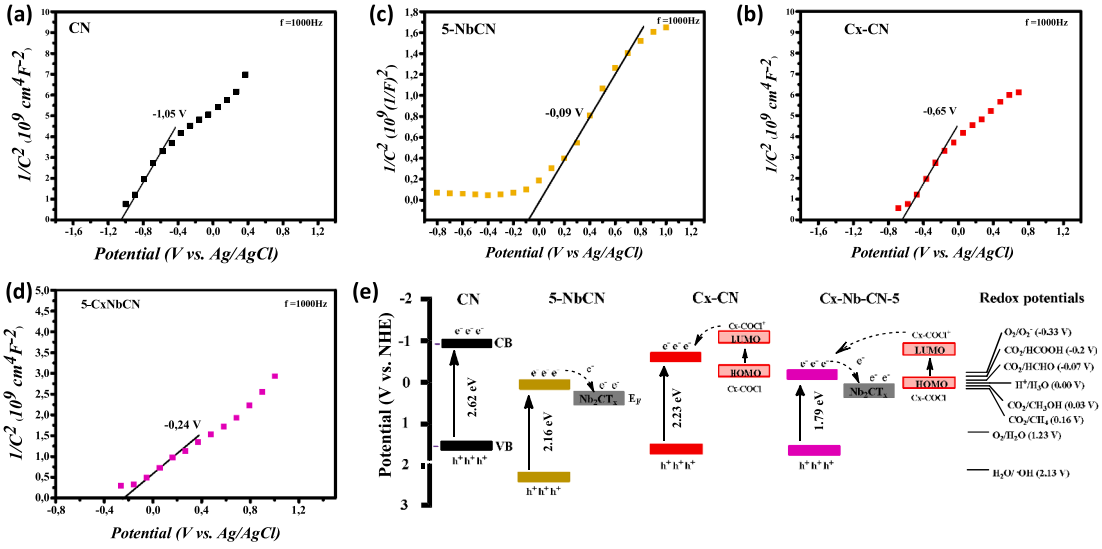


Fig. 4. Mott-Schottky plots (a-d) and the photocatalytic band potential diagram (e) for CN, 5-NbCN, CxCN, and 5-CxNbCN.

Table 2
Photoelectronic properties of the as-synthesized photocatalysts.

Samples	UV–Vis Abs. edge (nm)	E_g (eV)	XPS_{VB} (eV)	E_{CB} (eV)	V_{fb} (V vs. Ag/AgCl)	V_{CB} (V vs. NHE)	V_{VB} (V vs. NHE)
CN	462 [b]	2.62 [b]	2.26 [b]	- 0.36 [b]	−1.05 [b]	−0.95 [b]	+1.67 [b]
5-NbCN	564 [a]	2.16 [a]	1.85 [a]	- 0.31 [a]	−0.09 [a]	+0.01	+2.17
Cx-CN	532 [b]	2.23 [b]	2.06 [b]	- 0.17 [b]	−0.65 [b]	−0.55 [b]	+1.68 [b]
5-CxNbCN	574 [b]	1.79 [b]	2.24 [b]	+ 0.45 [b]	−0.24 [b]	−0.14 [b]	+1.65

[a] Values obtained from ref [31].
[b] Values obtained from ref [32].

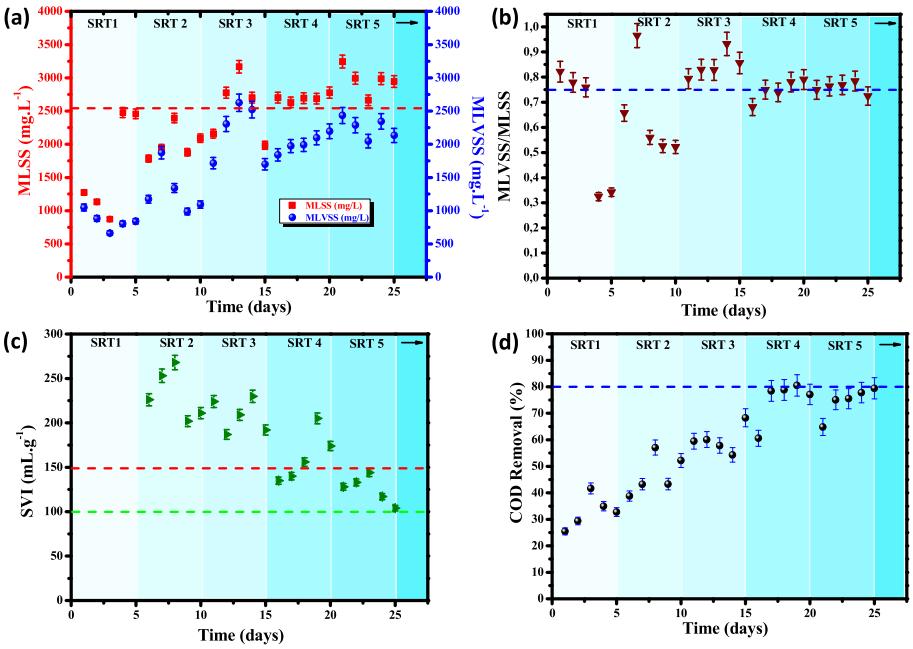


Fig. 5. Activated sludge parameters (a) MLSS and MLVSS, (b) ratio MLVSS/MLSS, (c) SVI, and (d) COD during the acclimatization; from real wastewater (SRT 1) to synthetic wastewater (SRT 5).

MLSSs and MLVSSs were ascribed to a change in the sludge environment from the real WWTP to the lab-scale WWTP, which suggests sludge deterioration. Moreover, the optimum range for MLSSs is between 2000 and 5000 mg.L^{-1}, and ideally 2500 mg.L^{-1} for traditional activated sludge WWTP [24]. The values gradually increased through SRT 2, were the MLSSs values reached the target of 2500 mg.L^{-1} in SRT 3. The stabilization of the MLSSs values during SRT 4 and 5 in the optimum range of 2500 mg.L^{-1} signifies continuous acclimatization of the activated sludge to the SWW. The MLVSSs values also increased gradually from SRT 4 to 5 during acclimatization, where the values reached about 70 to 80 % of the MLSSs which is desired for optimal activated sludge suspended matter [24]. Moreover, MLVSSs/MLSSs ratios in Fig. 5**(b)** were calculated to further assess the proportion and quality of microorganisms. Optimum activity of microorganisms in the activated sludge is characterized by the MLVSSs/MLSSs ratio, of which optimum values range between 0.7–0.8 [42]. MLVSSs/MLSSs ratio in SRT 1 (Fig. 5**(b)**) showed a notable decline from the desired range to 0.31, and gradually increased throughout SRT 3 to SRT 5 until optimum values ranging between 0.7 and 0.8 were reached. This confirms acclimatization of the microorganisms to the SWW and the lab-scale WWTP. On the other hand, the sludge volume index (SVI) was synchronously investigated to acquire insight into the colloidal settleability of the activated sludge in the clarifier unit. Generally, acceptable settleability SVI values range between

80 and 150 mL.g^{-1}, where excellent settleability is observed at <80 mL.g^{-1}, and sluggish settling at >150 mL.g^{-1} which is dependent on the sludge size and shape [43]. For the lab-scale WWTP used in this work, the targeted optimum SVI ranges were set to a minimum of 100 mL.g^{-1} (green line) and a maximum of 150 mL.g^{-1} (red line). As shown in Fig. 5 **(c),** the SVI data was acquired during the acclimatization process (SRT 2 to SRT 5). It is important to note that SVI data for SRT 1 was not presented since the waste activated sludge (WAS) needed for SVI was obtained after SRT 1. The SVI in Fig. 5**(c)** shows values above 150 mL.g^{-1} from SRT 2 to SRT 4 suggesting poor settleability. Moreover, the SVI reached optimum levels between 100 and 150 mL.g^{-1} during SRT 5, further signifying progress in the acclimatization process. Correspondingly, the biodegradability efficiency of the activated sludge was tested by measuring chemical oxidation demand (COD) in Fig. 5**(d)**. In the beginning of the acclimatization process, the COD removal percentage were significantly low (25.9 %) on day 1 of SRT 1. However, the COD removal gradually increased from SRT 2 to SRT 4, where the targeted 80 % COD removal was reached during SRT 4. The improved COD removal confirms improved microbial activity due to acclimatization of the activated sludge to the SWW influent. Overall, the MLSSs, MLVSSs, MLVSSs/MLSSs, SVI, and the COD removal data show continuous adaptation of the activated sludge to the new environment as the optimum targeted values are achieved during SRT 4 to SRT 5. At SRT 5, the influent entering the lab-scale WWTP is 100 % SWW which was used to gradually substitute domestic wastewater influent from Daspoort (Pretoria, South Africa) WWTP. Detailed acclimatization data including dissolved oxygen (DO), conductivity, and pH are outlined in **Table S3 (SI)**.

3.3. Bio-degradation of hydroxychloroquine sulfate and oseltamivir phosphate

After the configured lab-scale WWTP was acclimatized and it had reached a steady state, biodegradation efficiency of the microorganisms in the activated sludge were evaluated against HCQ and OS. The behaviour of the activated sludge suspended solids was evaluated in presence of the antiviral drugs HCQ followed by OS as shown in Fig. 6. Fluctuations in the MLSSs and MLVSSs were observed upon the introduction of HCQ (SRT 6) and OS (SRT 7), and this was attributed to a change in influent chemical composition which affects the growth of microorganisms in the activated sludge (Fig. 6**(a)**). Correspondingly, MLVSSs/MLSSs ratios also notably declined from 0.78 (day 27) to 6.32 (day 29) during biodegradation of HCQ (Fig. 6**(b)**). This activity shows deterioration of the microorganisms, however, the MLVSSs/MLSSs ratio increased to 0.67 (day 30) suggesting improved activated sludge quality thereafter. Furthermore, SVI plot in Fig. 6**(c)** for both HCQ (SRT 6) and OS (SRT 7) delineated oscillations within the optimum ranges between 100 and 150 mL.g^{-1}. The COD removal in the presence of the antiviral drugs significantly dropped from 80 % during the steady state (SRT 5) to the lowest COD removal of 37.3 % (SRT 6, day 27) (see Fig. 6**(d)**). However, the COD removal increased to 56.1 % (for OS) during day 30 (SRT 6), and this could be credited to the acclimatization of the activated sludge to the antiviral drugs in the influent.

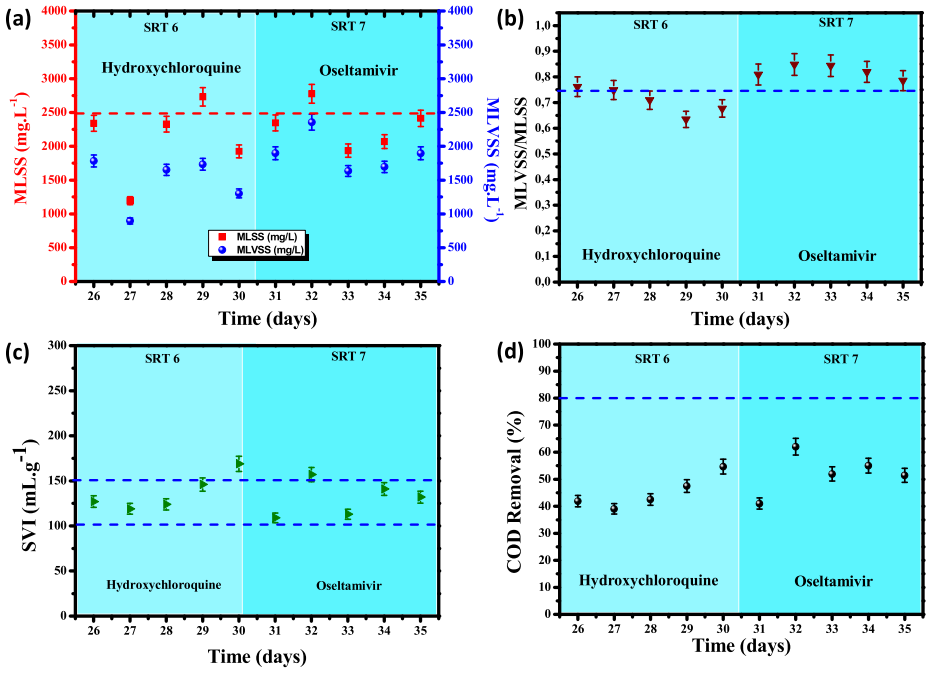


Fig. 6. Activated sludge parameters (a) MLSS and MLVSS, (b) ratio MLVSS/MLSS, (c) SVI, and (d) COD during biodegradation of hydroxychloroquine sulfate (SRT 6) and oseltamivir phosphate (SRT 7).

3.4. Photodegradation optimization hydroxychloroquine sulfate and oseltamivir phosphate

Optimizations of the photocatalytic reactor were conducted to understand the operation and consequently improve the photodegradation efficiency of pollutants. These optimization measurements were conducted to achieve optimal operational conditions in the photoreactor, which was later used for the treatment of biologically pre-

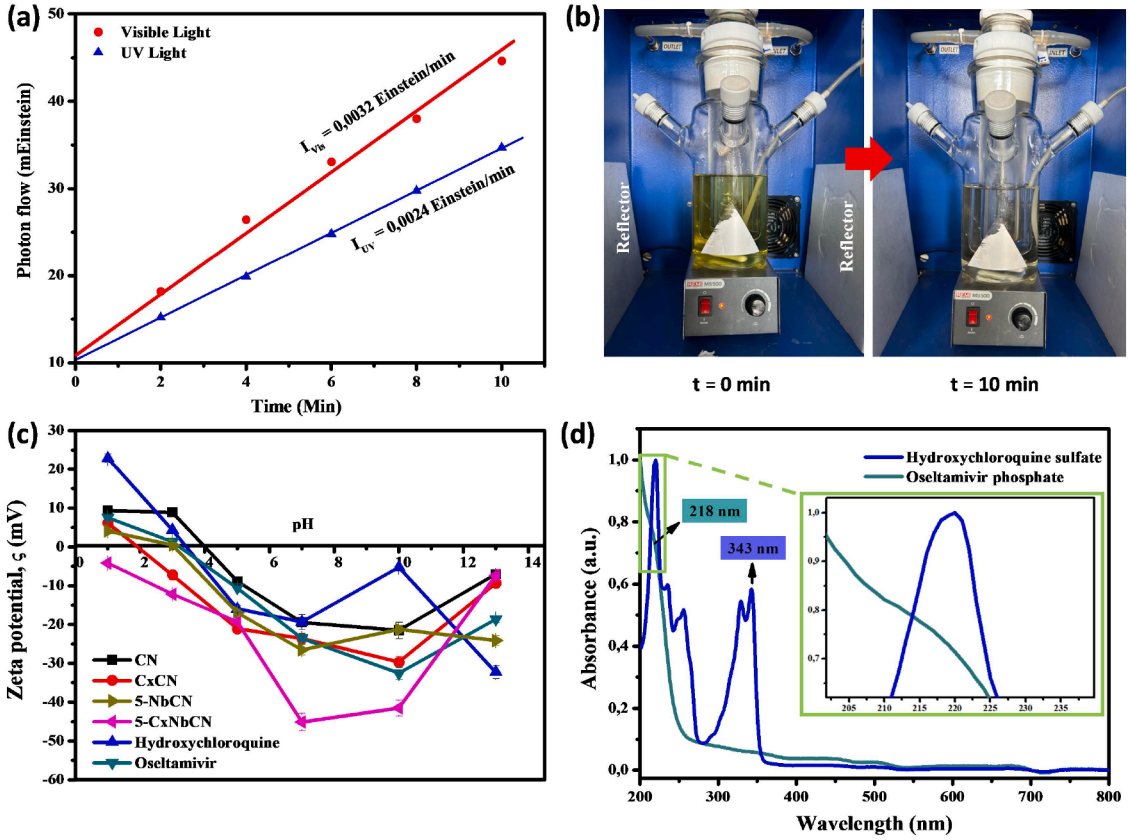


Fig. 7. The rate of photon flow under visible and UV lights (a), digital images of actinometric solution (b), Zeta potential as function of pH (c), and UV–Vis absorption spectra of hydroxychloroquine sulfate and oseltamivir phosphate in DI-H_2O (d). I_{Vis} and I_{UV} are photon flow due to ultraviolet and visible light, respectively.

treated wastewater. Initially, the light source irradiance was studied in the photoreactor by conducting photon flux measurements, following previously reported actinometrical studies [34,44]. The incident photon flow (I_0) as a function of irradiation time was obtained for a 250 W visible-light and a 250 W UV-light as shown in Fig. 7**(a)**, and the data was used to assess the rate of photon flow in the reactor. A visible light (250 W Xenon lamp) source presented a higher incident photon flow of $I_{Vis} = 3.2$ mEinstein.min^{-1} relative to the ultraviolet light with $I_{UV} = 2.4$ mEinstein.min^{-1}. Fig. 7**(b)** presents real time images of the photoreactor during photon flux measurements, where the yellow (pale) colour of the ferric sulphate solution turns colourless after 10 min of irradiation. Moreover, the observed colour change is a result of the reduction of ferric ions Fe^{3+} to ferrous ions Fe^{2+} upon light exposure. Polystyrene light reflectors were employed in the photocatalytic reactor to concentrate light intensity onto the glass reaction vessel (Fig. 7**(b)**).

Zeta potentials (ζ) as a function of solution pH were studied to evaluate surface charge and consequently deduce the point of zero charge (isoelectric point, ζ = 0 mV) (**Fig. 7(c)**). The net surface charge plays a crucial role in colloidal behaviour of nanomaterials, where a high ζ (> ± 30 mV) suggests higher electrostatic repulsion [32,45]. In **Fig. 7(c)**, it was observed that all the as-prepared materials exhibits less negative ζ values in the acidic (i.e. pH<4) media than in all the other pH ranges. This phenomenon could be attributed to the adsorption and protonation of the H^+ ions from the HCl solution [46]. It is worth noting that the ζ of all the materials drops until neutral pH is reached, at this point no HCl was used. The ζ gradually increases (becomes less negative) as the pH increases to a more alkaline solution, owing to the introduction of 0.1 M NaOH to the solution. The isoelectric point (ζ = 0 mV, pzc) for the as-prepared materials ranges from pH 2 to 5, including the pcz for HCQ (pzc pH = 3.34) and OS (3.02) antiviral drugs. A detailed discussion of the colloidal stability of the reported photocatalysts is outlined in our previous work [32]. The ultraviolet-visible (UV–Vis) absorption spectra of the antiviral drugs (HCQ and OS) are presented in **Fig. 7(d)**. Maximum optical absorption bands were obtained for HCQ at 343 nm and OS at 218 nm (See **Fig. 7(d)**). The obtained absorption bands were used as reference peaks for UV–Vis spectroscopy quantification of the pollutants during photodegradation.

The photodegradation efficiencies of the prepared photocatalysts were systematically evaluated against hydroxychloroquine (HCQ) sulfate and oseltamivir (OS) phosphate in deionised water and in synthetic wastewater (SWW). Several imperative parameters were taken into consideration to maximize the photocatalytic activity of the materials. These include, working solution pH, photocatalysts loading, and pollutant initial concentration. The optimization studies were conducted with solution working volume of 250 mL.

The potential of hydrogen (pH) plays an imperative role in photocatalytic degradation of pollutants in aqueous media. Generally, solution pH facilitates surface electrical charge attributes of photocatalysts and promotes the degree of ionization of the dispersed materials [47]. The photodegradation profiles of HCQ using the photocatalysts CN, CxCN, 5-NbCN, and 5-CxNbCN at different pH (1, 4, 7, 10, and 13) values are shown in Fig. 8. To evaluate the influence of pH, parameters such as catalysts loading and pollutant concentrations were kept at constant values of 5 mg and 5 mg.L^{-1}, correspondingly. Based on the data presented in Fig. 8, it can be observed that all the photocatalysts exhibit the highest photodegradation efficacy in acidic medium, specifically at pH 4 for 5-CxNbCN with 58.5 % degradation efficiency. The pH trend for 5-CxNbCN delineated is as follows; pH 4>pH 1>pH 7>pH 10>pH 13, where pH 13 exhibited the least activity of 25.7 % degradation after 60 min of irradiation. Additionally, all the other photocatalysts CN, CxCN, and 5-NbCN exhibited photodegradation activity of up to 39.9 %, 47.8 %, 56.0 % respectively at pH 4 (indicated by red curves in Fig. 8). The observed general trend suggests that the photodegradation activity increases with a decrease in the pH of the working solution. This phenomena can be attributed to two factors; (i) isoelectric point (pzc, ζ = 0 mV) and (ii) pollutants dissociation constants (pKa). In acidic medium (pH ~4), the pollutants HCQ and OS and the photocatalysts CN, CxCN, 5-NbCN, and 5-CxNbCN present ζ values closest to the respective pzc values, suggesting potential adsorption of the pollutants onto the photocatalysts. The adsorption of the pollutant (HCQ) by the photocatalyst in the dark can distinctly be seen in Fig. 8**(d)** at pH 4, where up to 15.6 % of the pollutant was adsorbed. Furthermore, the highest adsorptions in the dark presented in Fig. 8**(b)** and Fig. 8**(d)** can be credited to host-guest complexation facilitated by the calixarene-based catalysts.

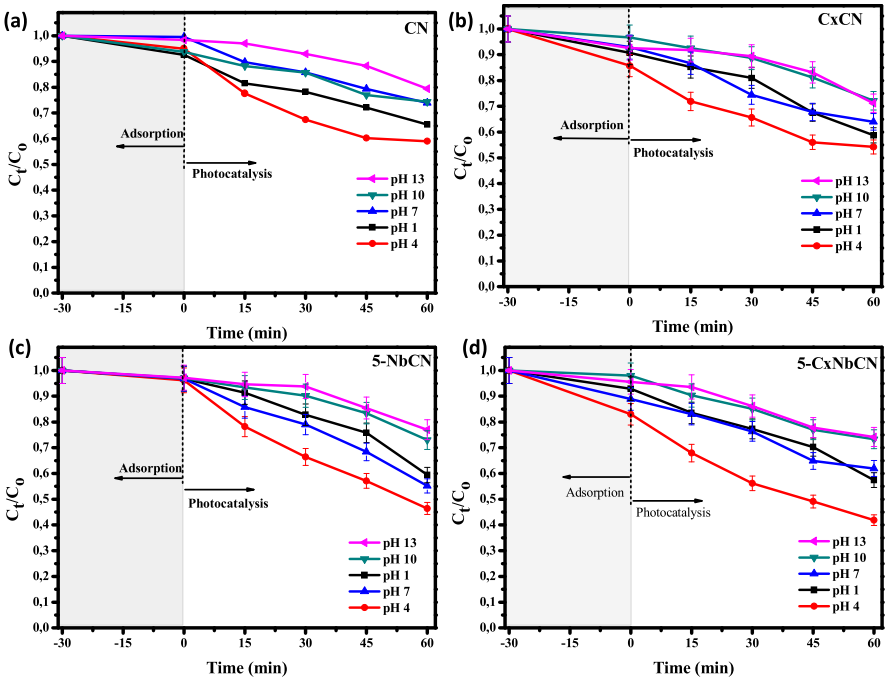


Fig. 8. Effects of solution pH towards photodegradation of hydroxychloroquine sulfate (5 mg.L^{-1}) using (a) CN, (b) CxCN, (c) 5-NbCN and (d) CxNbCN photocatalysts (5 mg): pH optimizations.

Factoring in the pKa values of the pollutants, HCQ possesses three typical basic functional groups with pKa values <4.0, 8.3 and 9.7, suggesting possibility of partial protonation to cation in acidic medium [48]. At low pH values (lower than the pKa), the pollutants are prone to dissociations which could facilitate electrostatic attractions with the photocatalysts. Similarly, OS possesses pKa value of 7.7 on its primary amine, signifying the possibility of protonation in acidic medium [49]. The formations of HCQ and OS cations in acidic medium facilitate the electrostatic interaction with partial positively charged photocatalysts, and consequently improving adsorption processes. The changes in surface charge in the acidic and basic medium for the photocatalyts were explained through Eq. (3) and 4.

$$\text{Catalyst} - \text{OH} + H^{+} \rightarrow \text{Catalyst} - \text{OH}_2^{+} \ (\text{pH} < \text{pzc}) \quad (3.1)$$

$$\text{Catalyst} - \text{OH} + \text{OH}^{-} \rightarrow \text{Catalyst} - \text{O}^{-} + \text{H}_2\text{O} \ (\text{pH} > \text{pzc}) \quad (4)$$

Where Eq. (3) outlines the formation of partial cations in acidic media where pH is less than the pzc. The formation of partial positively charged photocatalysts in the acidic medium is as a result of protonation with the H^{+} ions from the HCl in the solution. Moreover, Eq. (4) delineates the deprotonation and the formation of partial negatively charged anions on the photocatalysts in basic (NaOH was used) environment, thus resulting in negative ζ values. The improved pollutants adsorption by the photocatalysts in the acidic medium could be due to the fact that the pollutants exhibit high ζ relative to the photocatalysts, thus allowing electrostatic interactions.

Photocatalyst loading plays a crucial role in the overall activity of the photodegradation of the pollutants in water. It has been reported in several studies that the increase in catalyst loading to a certain extend is directly proportional to the photodegradation efficiency [12,20,28]. Hence, it is imperative to explore the optimum loading of the photocatalyst at constant pH and pollutant concentration. Furthermore, it is important to conduct optimization of photocatalyst concentration to avoid excess catalyst which could lead to competition for photon absorption. Moreover, the use of optimum amounts of photocatalysts could be beneficial in reducing the operation costs. In Fig. 9, the photocatalytic activities of all the materials were observed to be directly proportional to the photocatalyst loading concentration from 5 to 20 mg. The highest photodegradation efficiency of 80.1 % was observed for 20 mg of 5-CxNbCN, whilst 5 mg of 5-CxNbCN presented an efficiency of 44.8 % (Fig. 9**(d)**). Similar trends were observed where 5 mg exhibited the least performance relative to the 20 mg loading of the photocatalysts (Fig. 9). This phenomenon can be attributed to the fact that increasing photocatalyst loading facilitates catalytically active sides for redox reaction. Furthermore, the increased catalyst loading can also lead to more reactive oxygen species generated from the photoinduced charge carriers. However, it is worth noting that excess loading could result in light shielding due scattering, which could negatively impact the photodegradation process [50].

To investigate the effect of initial pollutant concentrations, the optimum pH 4 and photocatalyst concentration of 20 mg were maintained. The pollutant concentrations and the photocatalysts loading have a close ration, since high concentrations of pollutants would compete for adsorption on the surface of photocatalyst. The data for the effect of initial pollutant concentrations on the degradation is presented in Fig. 10. It is worth noting that increasing the starting pollutant concentration inversely decreases the photodegradation efficiencies for all the photocatalysts (Fig. 10). In Fig. 10**(d)**, the highest degradation efficiencies were observed for 5-Cx-Nb-CN in the order from 5 (79.9 %), 10 (68.5 %), 15 (51.5 %), and the least was observed for 20 mg.L^{-1} (29.7 %). The observed decrease in photodegradation activities in high pollutant concentrations could be attributed to absorption of incident light by the pollutant before reaching the surface of the photocatalyst [20,50]. Similar trends were observed for CN, CxCN, and 5-NbCN, as delineated in Fig. 10. Additionally, the pollutants could be competing for the generated reactive oxygen species (ROS). Nonetheless, the optimum operating conditions of the photocatalytic processes were obtained to be as follows; pH 4, photocatalyst loading 20 mg, and pollutant concentration of 5 mg.L^{-1} in a working volume of 250 mL.

The photocatalytic degradation efficiency of the as-synthesized materials CN, CxCN, 5-NbCN, and 5-CxNbCN were evaluated towards the degradation of hydroxychloroquine sulfate (HCQ) and oseltamivir phosphate (OS). The optimization of the photocatalytic reactor conditions were conducted using only HCQ, and this was due to the fact that the two pollutants (HCQ and OS) presented similar surface charge (both have pzc at pH 4) and pKa trends. The ζ graphs of both the pollutants follow same trends, where they present positive ζ values in acidic media (pH<pzc) and become negative in basic media (pH>pzc). Therefore, the

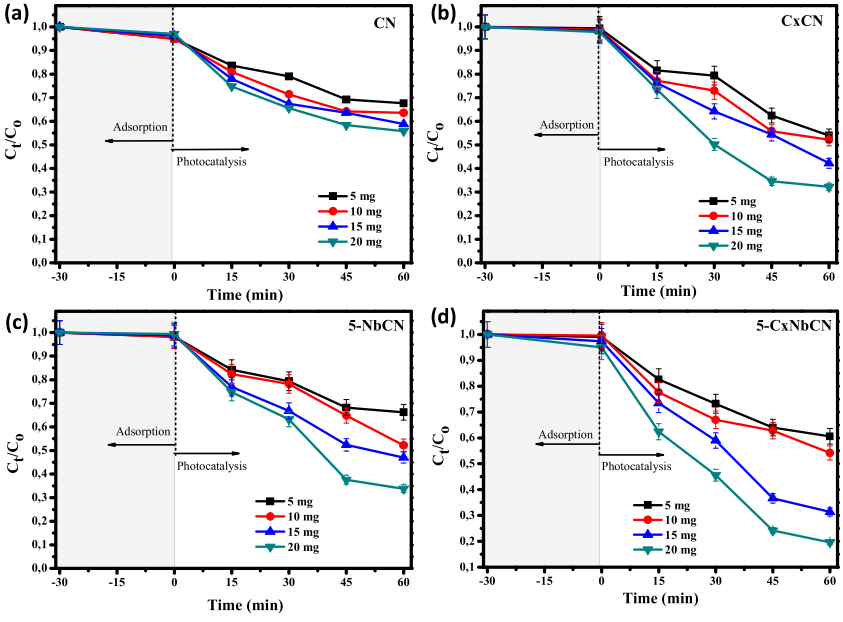


Fig. 9. Effects of photocatalyst loading (5 mg to 20 mg) towards the photodegradation of hydroxychloroquine sulfate (5 mg/L) using (a) CN, (b) CxCN, (c) 5-NbCN and (d) 5-CxNbCN at optimum pH (4): catalyst loading optimizations.

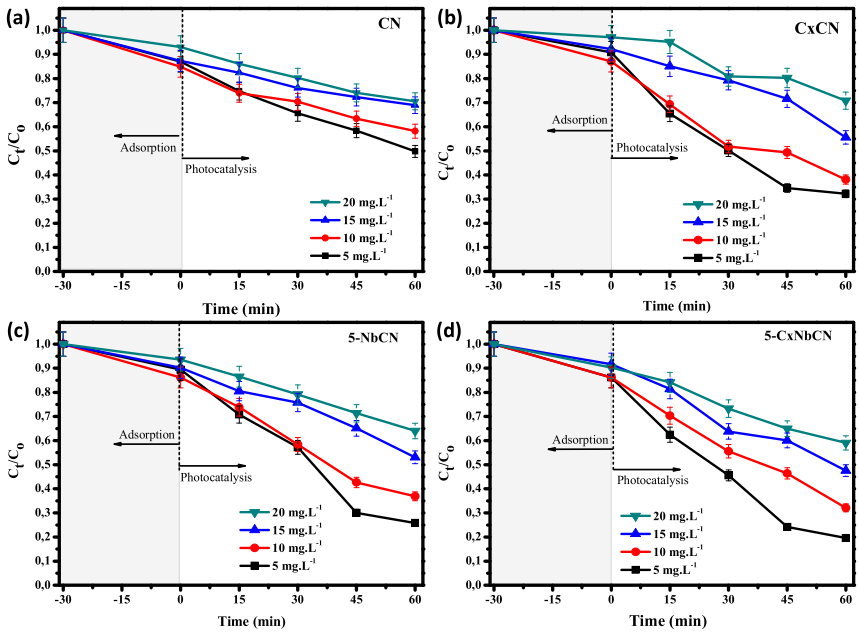


Fig. 10. Effects of initial concentration of pollutant towards photodegradation of hydroxychloroquine sulfate (5 to 20 mg.L^{-1}) using (a) CN, (b) CxCN, (c) 5-NbCN and (d) 5-CxNbCN photocatalysts (20 mg) at optimum pH 4: pollutant concentration optimization.

optimum degradation conditions of 20 mg catalyst loading, 5 mg.L^{-1} pollutant concentrations and a working pH of 4 were used for both the pollutants (HCQ and OS). The optimizations were conducted using a 250 W visible light, and the photocatalytic performances of the materials will later be conducted under 250 W ultraviolet (UV) light using the same optimal photoreactor conditions. The different light sources (visible and UV lights) were used to assess the materials photocatalytic activities under different incident photon energy.

Fig. 11**(a)** and **(d)** presents a comparison of the photodegradation ability of the photocatalysts towards HCQ and OS under visible light irradiation, respectively. Self-photolysis of the pollutants (HCQ and OS) were also assessed under visible light irradiation, which showed good photostability, evident by the negligible changes over 60 min of irradiation (Fig. 11**(a)** and **(d)**). Adsorption-desorption for both HCQ and OS were also established by carrying out the dark experiments for 30 min (Fig. 11**(a)** and **(d)**). A higher adsorption efficiency of 15 % was observed for the 5-CxNbCN against OS, whilst 6 % was observed for 5-CxNbCN against HCQ. The improved adsorption for 5-CxNbCN and CxCN relative to the CN and 5-NbCN is attributed to the presence of calixarene host-guest molecules. Adsorption of pollutants onto the surface of the photocatalysts is a prerequisite for efficient photocatalytic degradation. Upon visible irradiation, the three-component photocatalyst 5-CxNbCN displayed excellent photocatalytic activity of 81.5 % and 67.2 % for HCQ and OS (Fig. 11**(a)** and **(d)**), correspondingly. The

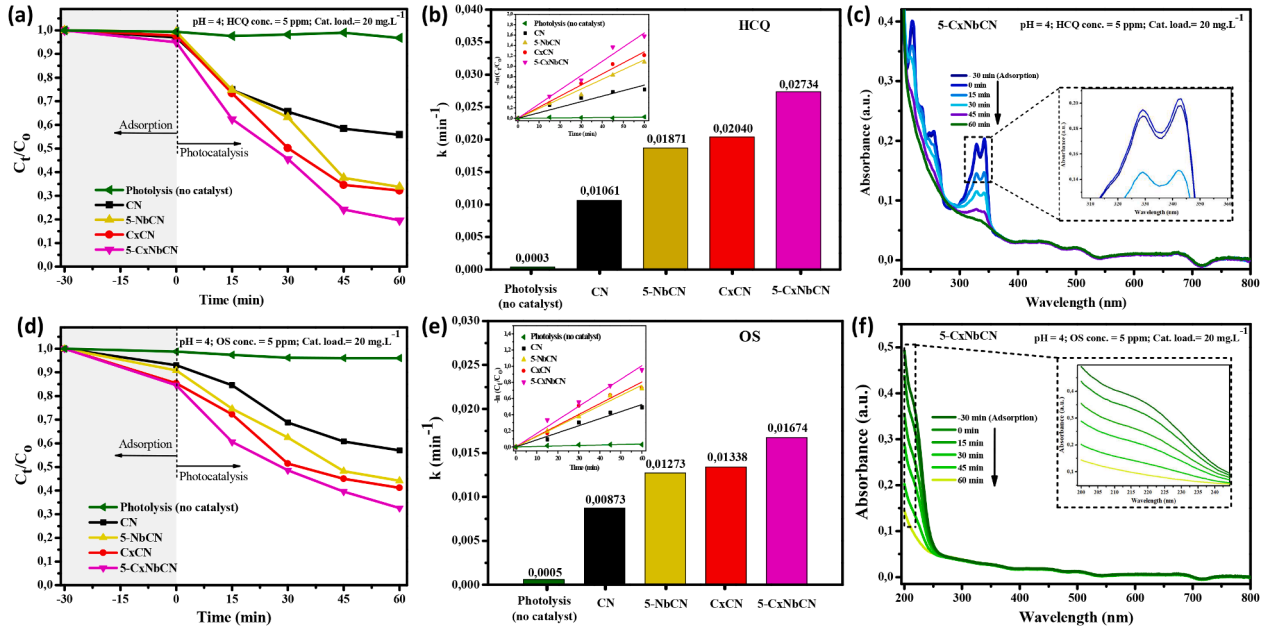


Fig. 11. Photocatalysts comparison towards the photodegradation of hydroxychloroquine sulfate (HCQ) and oseltamivir phosphate (OS) under visible light; (a,d) photodegradation curves (b,e), degradation kinetics and rate constants, (c,f) UV–Vis absorption spectrum as a function of irradiation time.

least photocatalytic activity was observed CN, where the removal efficiency of 43.5 and 41.2 % were obtained for HCQ and OS, correspondingly. The lower photocatalytic performances of CN compared to 5-CxNbCN could be credited to a combination of factors such as rapid electron-hole pair recombinations, poor charge conductivities, and inefficient charge carrier separations and transfers [28,29]. Meanwhile, excellent light utilization rates and efficient separation of photoinduced charge carriers were observed for 5-CxNbCN compared to CN, CxCN, and 5-NbCN, which showed a positive impact on the overall photocatalytic performances.

Photodegradation kinetics were also conducted to evaluate the removal reaction rates of HCQ and OS using 5-CxNbCN. The reaction kinetics were studied using Langmuir-Hinshelwood pseudo-first-order kinetic formula reported elsewhere, Eq. (3) [15]. The graphs in Fig. 11 **(b)** and **(e)** present the reaction kinetics following the pseudo-first-order for HCQ and OS, respectively. Linear regression was employed to deduce the apparent rate of reaction (inserts in Fig. 11**(b)** and **(e)**) from the photodegradation data. In Fig. 11**(b)**, the ternary composite 5-CxNbCN possesses significantly higher reaction rate constant of 2.73×10^{-2} min^{-1} towards HCQ. The lowest reaction rate constant of

1.06×10^{-2} min^{-1} was observed for the pristine CN towards the degradation of HCQ, which is 2.6 times less than that for 5-CxNbCN (Fig. 11**(b)**). The order of reaction rate constant for the photocatalysts against HCQ were as follows; CN ($k = 1.06 \times 10^{-2}$ min^{-1})< 5-CxNb ($k = 1.87 \times 10^{-2}$ min^{-1})< CxCN ($k = 2.04 \times 10^{-2}$ min^{-1} < 5-CxNbCN ($k = 2.73 \times 10^{-2}$ min^{-1}). Similar trends in the reaction rate constant of the as-prepared materials against OS were observed in Fig. 11**(e)**, where the highest reaction rate constant was observed for 5-CxNbCN ($k = 1.67 \times 10^{-2}$ min^{-1}). Comparing CxCN to 5-NbCN, the reaction rate constants for the two are relatively close towards the degradation of both HCQ and OS. This could be ascribed to their closely related optoelectronic properties. Additionally, the UV–Vis absorption optical spectra for the photodegradation of HCQ and OS using 5-CxNbCN are delineated in Fig. 11 **(c)** and **(f)**. Significant changes in the absorption bands were observed for both the pollutants, where the absorption bands almost completely disappeared after 60 min of visible light irradiation. The continuous reduction in the UV–Vis absorption bands at λ_{max} suggests the photodegradation of the pollutants and this was later confirmed by LC-MS analyses.

3.5. Coupled bio-photo degradation of hydroxychloroquine sulfate and oseltamivir phosphate

A coupled bio-photodegradation system was utilized under acclimatized and optimum conditions for the complete obliteration of antiviral drugs (HCQ and OS) from wastewater. The pollutants were pretreated through biodegradation using activated sludge in a lab-scale wastewater treatment plant (WWTP), followed by photocatalytic treatment using 5-CxNbCN under the optimum photoreactor conditio. The photocatalysts 5-CxNbCN was used in the photoreactor system since it presented the highest degradation ability relative to CN, CxCN and 5-NbCN. Synthetic wastewater was employed in the biodegradation process to mimic the environmental water metrics. In real wastewater, the antiviral drugs naturally co-exist with a wide range of organic and inorganic materials including inorganic ions [15]. It's important to note that the activated sludge system was employed as the first step in the water treatment process to remove all suspended and biodegradable pollutants from wastewater before the photocatalytic treatment of dissolved antiviral drugs. This approach was taken to prevent light obstruction caused by suspended colloidal particles during photocatalysis.

The bio-photodegradation curves for HCQ and OS are outlined in Fig. 12**(a)**, and the corresponding UV–Vis absorption spectra are shown in Fig. 12**(b)** and **(c),** respectively. All operating conditions for the hyphenated bio-photocatalytic system were as derived from the optimization studies for both the HCQ and OS antiviral drugs. In Fig. 12**(a)**, the lab-scale WWTP biodegradation process exhibited a reasonable degradation efficiency of 62.5 and 58.1 % for HCQ and OS, correspondingly. Upon the photocatalytic treatment of HCQ and OS using 5-CxNbCN irradiation with visible light, the degradation efficiency increases to 97.3 and 92.6 %, respectively. The observed remarkable degradation efficiency signifies the excellent performances of the hyphenated treatment system for the removal of the antiviral in real wastewater. The UV–Vis absorption spectra in Fig. 12**(b)** and **(c)** also presents a notable degradation of HCQ and OS, respectively. The reaction rate constants were also delineated in Fig. 12**(d)**, where HCQ and OS presented high reaction rate constants of 3.23×10^{-2} and 2.51×10^{-2} min^{-1}, respectively. The COD removal measurements following the bio-photo degradation of HCQ and OS were replaced by the LC-MS measurements for a more specific analysis of the decompositions of HCQ and OS, as discussed later in the manuscript.

The effects of different light sources towards the photodegradation of HCQ and OS were also investigated using UV and visible light sources as shown in Fig. 12**(e)**. The comparative studies of the light sources were also conducted using 5-CxNbCN under the optimized photocatalytic parameters. It is worth noting that the visible light presented relatively higher degradation efficiencies of 77.8 and 69.4 % for HCQ and OS, correspondingly. Moreover, relative lower photocatalytic performances were observed for the UV light with degradation efficiencies of 63.6 and 51.6 % for HCQ and OS, correspondingly (Fig. 12**(e)**). The observed phenomenon is in agreement with the photon flux measurement, where the visible light presented higher photon flow (I_o= 3.2 mEinstein.min^{-1}) compared to the UV light (I_o= 2.4 mEinstein.min^{-1}). Additionally, the corresponding reaction kinetics for the light source comparisons were outlined in Fig. 12**(f)**, derived through pseudo-first-order (Insert in Fig. Fig. 12**(f)**). Visible light exhibited a higher rate constant of 2.54×10^{-2} min^{-1} for the degradation of HCQ, followed by 2.02×10^{-2} min^{-1} for OS using visible light.

3.6. Radical-trapping experiments and photocatalytic mechanism

In an effort to gain insights into the photodegradation mechanism and the involved reactive oxygen species (ROS), radical quenching experiments were conducted using a series of ROS scavengers. The used reagents for redox quenching studies includes p-benzoquinone (p-BQ), potassium dichromate ($K_2Cr_2O_7$), 2-propanol, and ethylenediaminetetraacetic acid (EDTA) acting as superoxide radicals ($\bullet O_2^-$), electrons (e^-), hydroxyl radicals (•OH), and holes (h^+) trapping agents respectively [51,52]. Fig. 13**(a)** presents the effect of a sequence of ROS scavengers on the photodegradation efficiency of HCQ after 60 min of visible light irradiation using the as-prepared 5-CxNbCN composite. In the absence of scavengers (denoted control), the removal efficiency of HCQ was 80.8 %, and dropped slightly to 78.0 % in the presence of EDTA (h^+ scavenger) (Fig. 13**(a)** and **(b)**). Moreover, a significant decrease in photodegradation of HCQ to 63.2, 46.4, and 30.7 % in the presence of 2-propanol (•OH quencher), $K_2Cr_2O_7$ (e^- quencher), and p-benzoquinone ($\bullet O_2^-$ quencher) were observed, respectively (Fig. 12**(a)** and **(b)**). The ROS responsible for the degradations of OS were also assessed using similar radical quenchers as in HCQ and the data was presented in **Fig. S2.** A similar trend was observed for the radical trapping experiments in OS, where the lowest degradation efficiency of 30.2 and 37.6 % were observed when p-benzoquinone ($\bullet O_2^-$ quencher) and $K_2Cr_2O_7$ (e^- quencher) were used, respectively (**Fig. S2 (a)** and **(b)**). In the absence of radical quenchers, the degradation efficiency of 75.6 % for OS was obtained (**Fig. S2 (a)** and **(b)**). The observed decrease in the photodegradation efficiency in the presence of scavengers signifies the competition for ROS between the pollutants and quenchers. Nonetheless, the presented data proves the participation of the e^-, •OH, and $\bullet O_2^-$ generated by the 5-CxNbCN, however the e^- and $\bullet O_2^-$ are the major contributing species towards decomposition of HCQ and OS. The corresponding reaction kinetics for HCQ and OS are presented in Fig. 13**(c)** and **Fig. S2 (c)**, derived from pseudo-first-order kinetic model. In Fig. 13

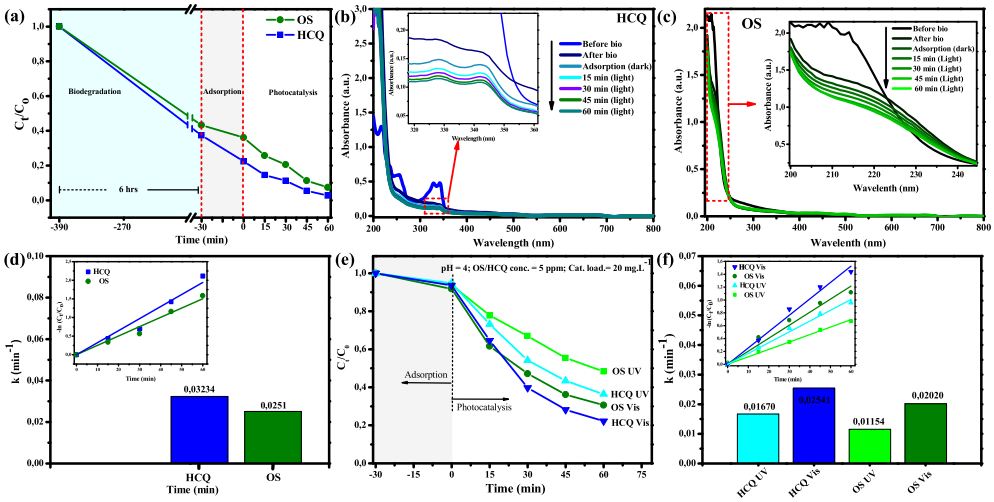


Fig. 12. (a) Bio-photo degradation curve of hydroxychloroquine sulfate (HCQ, 5 mg/L) and oseltamivir phosphate (OS, 5 mg/L) under visible light, (b) UV–Vis absorption spectra of HCQ, (c) UV–Vis absorption spectra of OS, (d) degradation kinetics and rate constants, (e) degradation curves under UV and visible lights, (f) degradation kinetics and rate constants for UV and visible lights .

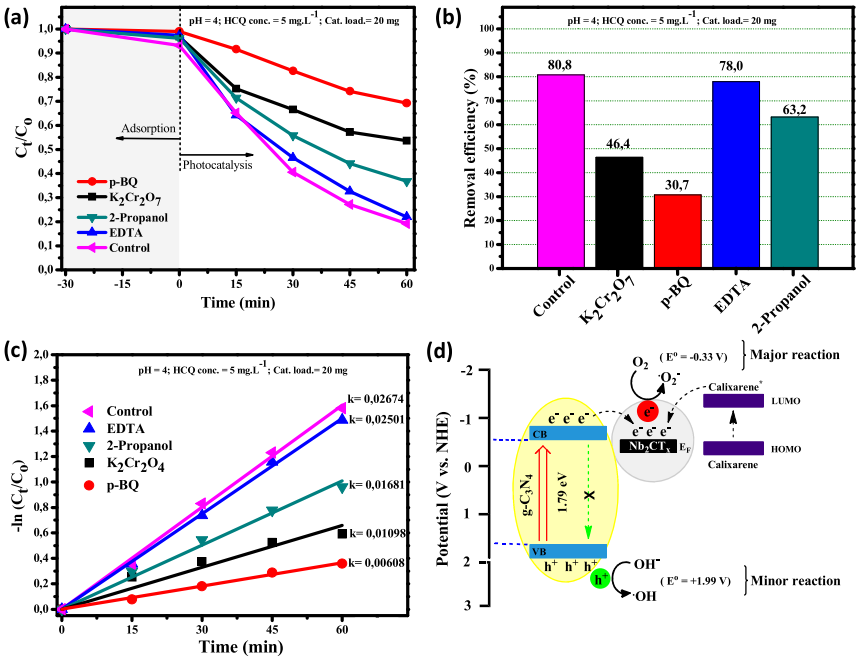


Fig. 13. (a) Photocatalytic degradation curves of HCQ using a series of radical scavengers, (b) HCQ comparative degradation efficiencies, (c) HCQ degradation rate constants, and (d) photocatalytic band diagram for 5-CxNbCN.

(c), the lowest reaction rate constant of 0.00608 min^{-1} was observed in the presence of p-benzoquinone, validating the major role constituted by the $\bullet O_2^-$ in the photodegradation of HCQ. Moreover, the degradation of OS in the presence of p-benzoquinone also showed the least activity with reaction rate constant of 0.00653 min^{-1} (**Fig. S2(c)**).

The photocatalytic band diagram was derived to delineate the possible interfacial charge carrier pathways and transfers in the calixarene-sensitized Schottky-junction 5-CxNbCN (See Fig. 13**(d)**). In Fig. 13**(d)** supported by the photoelectrochemical properties, it was observed the pristine g-C_3N_4 undergoes photoinduced charge carrier recombination, thus negatively affecting the generation of useful ROS. This phenomenon was resolved by incorporation of Nb_2CT_x MXene complex, followed by the introduction of a calixarene complex as light-sensitizer. The schematic in Fig. 13**(d)** visualizes the proposed charge transfer mechanism, where the electrons from the valence band (VB) of the g-C_3N_4 are photoexcited to the conduction band (CB), followed by migration onto the Nb_2CT_x MXene Fermi level (E_F). Calixarene molecules undergo photoexcitation from the highest occupied molecular orbital (HOMO) to the least unoccupied molecular orbital (LUMO) upon light irradiation, facilitating sensitization effect to the Schottky-junction (Fig. 13**(d)**) [53]. The photoinduced e^- (on the Fermi level of Nb_2CT_x) and holes (on the VB of g-C_3N_4) facilitate the generation of ROS in the presence of molecular oxygen (O_2) and H^+ ions. The generated ROS initializes the degradation of the pollutants (HCQ and OS) in solution. Eq. (5) **to** Eq. (9) below summarizes the above ROS generation discussion.

$$5\text{-CxNbCN} + h\nu \rightarrow 5\text{-CxNbCN}^* \ (h^+_{(\text{VB g-C3N4})} / \ e^-_{(\text{Fermi Nb2CTx})}) \ () \qquad (5)$$

$$e^{-}_{(Fermi\ Nb2CTx)} + O_2 \rightarrow \bullet O_2^{-}\ () \quad (6)$$

$$\bullet O_2^{-} + H^{+} \rightarrow \bullet OH\ () \quad (7)$$

$$h^{+}_{(VB\ g\text{-}C3N4)} + OH^{-} \rightarrow \bullet OH\ () \quad (8)$$

$$h^{+}/e^{-}/\bullet OH/\ \bullet O_2^{-} + HCQ/OS \rightarrow \text{photodegradation products}\ () \quad (9)$$

The fabricated photocatalytic nanocomposite 5-CxNbCN presented enhanced charge separation and transfers, thus leading to effective production of ROS for catalytic reactions.

To further evaluate the performances of the as-synthesized photocatalysts 5-NbCN, CxCN, and 5-CxNbCN relative to previously reported catalysts, graphitic carbon nitride (g-C_3N_4)-based photocatalysts were compared with the studied photocatalysts. The materials were compared based on the following variables; reaction conditions (name of pollutant, initial pollutant concentration and catalyst loading, solution pH), light source, irradiation times, pollutant removal efficiency, rate of reaction, and involved redox reactions. The catalysts performance comparison against selected pharmaceutical pollutants is presented in Table 3. It is worth noting that presented photodegradation efficiency of the current work under optimum conditions was comparable to recent studies on MXene and g-C_3N_4-based photocatalysts (Table 3). The as-prepared Calixarene@Nb_2CT_x@g-C_3N_4 catalyst showed degradation rate of 81.5 % (0.02734 min^{-1}) and 67.2 % (0.02734 min^{-1}) after 60 min of irradiation using significantly low catalyst loading of 20 mg. In addition, the developed photo-bio degradation system in this work presented remarkable removal efficiency of 97.3 % and 92.6 % against HCQ and OS with the corresponding reaction rate of 0.03234 and 0.02510 min^{-1}. The above data suggests the positive effect brought about by hyphenating the biodegradation with the photodegradation processes toward effective removal of pharmaceuticals from wastewater.

3.7. Photostability and recyclability

Photodegradation efficiencies of the optimized 5-CxNbCN were conducted over five cycles, this was to evaluate the materials reusability and stability under prolonged exposure to light and antiviral drugs (HCQ and OS). The recyclability studies were also conducted under the optimized photocatalytic parameters pH 4, pollutant concentration 5 $mg.L^{-1}$, and catalyst loading 20 mg using visible light. Fig. 14**(a)** and **(b)** shows the photodegradation curves and degradation efficiencies of 5-CxNbCN against HCQ over 5 cycles. Initial HCQ removal efficiency of 81.6 % was observed in the 1st cycle. After completion of the 5th cycle, the degradation efficacy slightly lowered with a decay of 13.8 %, revealing a good photostability of the as-prepared photocatalyst (Fig. 14**(b)**). The recyclability of the 5-CxNbCN photocatalyst was also evaluated during the photodegradation of OS (**Fig. S3**). In the 1st cycle of photodegradation of OS, the removal efficiency of 76.8 % was obtained, and declined to 72.4 % by the 5th cycle. The photodegradation of OS only declined with 4.4 % when comparing cycle 1 with 5. Additionally, XRD and SEM analytical techniques were used to further confirm the chemical and structural stability of the photocatalyst (Fig. 14**(c)** and **(d)**). The XRD spectra of the material before and after 5 cycles exhibited no apparent distortion in the characteristic peaks, thus amplifying good chemical stability. The slight increase in intensity of the calixarene amorphous peak between 10° and 20 ° 2θ could be attributed to the host-guest complexation with the antiviral drugs. SEM images in Fig. 14**(d)** exhibits characteristic morphology of 5-CxNbCN composite, which shows no changes after 5 cycles of photodegradations. Additional SEM images and EDS spectra for 5-CxNbCN before and after 5 cycles of OS degradation are presented in **Fig. S4**. This stability data confirms the robustness and recyclability of the as-prepared photocatalysts towards the photocatalytic degradation of the antiviral drugs (HCQ and OS).

3.8. Degradation pathways and byproducts

To study and identify the pollutants (hydroxychloroquine sulfate and oseltamivir phosphate) photodegradation complex intermediates, the liquid chromatography mass spectrometry (LC-MS/MS, Shimadzu 8030) analytical technique was employed (details on the SI). Total ion count (TIC) of mass chromatographs of different irradiation times (from t = 0 min to t = 120 min) using calixarene@Nb_2CT_x@g-C_3N_4 with initial pollutant (HCQ and OS) concentration of 5 mg/L at pH of 4 are shown in **Fig. S5**. It is worth noting that the TIC graphs in **Fig. S5** for OS show a reduction in the peak marked with dashed box. Similarly, the TIC of the mass chromatographs for HCQ also presented a complete disappearance of peak marked with dashed box. These observations in the narrowing and disappearance of the HCQ and OS TIC peaks suggest the decomposition of the parent complexes during photocatalysis. The corresponding HCQ and OS retention time peaks of the TIC chromatographs after 120 min of irradiation are delineated in **Fig. S6 (a and b)**.

The LC-MS/MS method reported in previous studies was modified and used to resolve HCQ and OS photodegradation intermediates and consequently deduce decomposition pathways [12,58,59]. The

Table 3
Comparison of MXene and g-C_3N_4-based photocatalysts towards the removal of pharmaceutical pollutants in waster.

Photocatalyst	Photocatalyst configuration	Pollutant	Photoreactor conditions	Irradiation times (min)	Removal efficiency (%)	Reaction rate (min^{-1})	Ref.
Calixarene@Nb_2CT_x@g-C_3N_4	Sensitized Schottky-junction	Hydroxychloroquine sulfate (5 ppm)	250 W Xe lamp; pH = 4; Cat. loading = 20 mg	60	81.5	0.02734	In this study
Calixarene@Nb_2CT_x@g-C_3N_4	Sensitized Schottky-junction	Oseltamivir phosphate (5 ppm)	250 W Xe lamp; pH = 4; pH = *N*/A; Cat. loading = 20 mg	60	67.2	0.01674	In this study
g-C_3N_4/Ti_3C_2/ Ag_3PO_4	S-scheme	tetracycline hydrochloride (20 ppm)	300 Xe lamp; Cat. loading = 30 mg in 50 mL (600 ppm)	60	88.4	0.03525	[28]
Bi/BiOBr/P@g-C_3N_4	S-Scheme	Levofloxacin (10 ppm)	90 W LED; pH = 6.32; Cat. loading = 0.1 g/L (100 ppm)	70	77.2	0.0427	[54]
Bi/BiOBr/P@g-C_3N_4	S-Scheme	Oxytetracycline (10 ppm)	90 W LED; pH = 6.32; Cat. Loading = 0.1 g/L (100 ppm)	70	69.8	0.0224	[54]
$Ti_3C_2T_x$/alkalized g-C_3N_4	Schottky-junction	Tetracycline hydrochloride (20 ppm)	300 W Xe lamp; pH = *N*/A; Cat. loading = 10 mg in 50 mL (200 ppm)	60	77.0	0.0307	[55]
g-C_3N_4/Ti_3C_2	Schottky-junction	Ciprofloxacin (20 ppm)	500 W Xe lamp; pH = *N*/A; Cat. loading = 10 mg in 50 mL (200 ppm).	150	100	0.0350	[56]
Ti_3C_2/g-C_3N_4 (MX/CN)	Schottky-junction	Ciprofloxacin (10 ppm)	300 W Xe lamp; pH = 7; Cat. loading = 200 mg in 100 mL (2000 ppm)	210	97.98	–	[57]

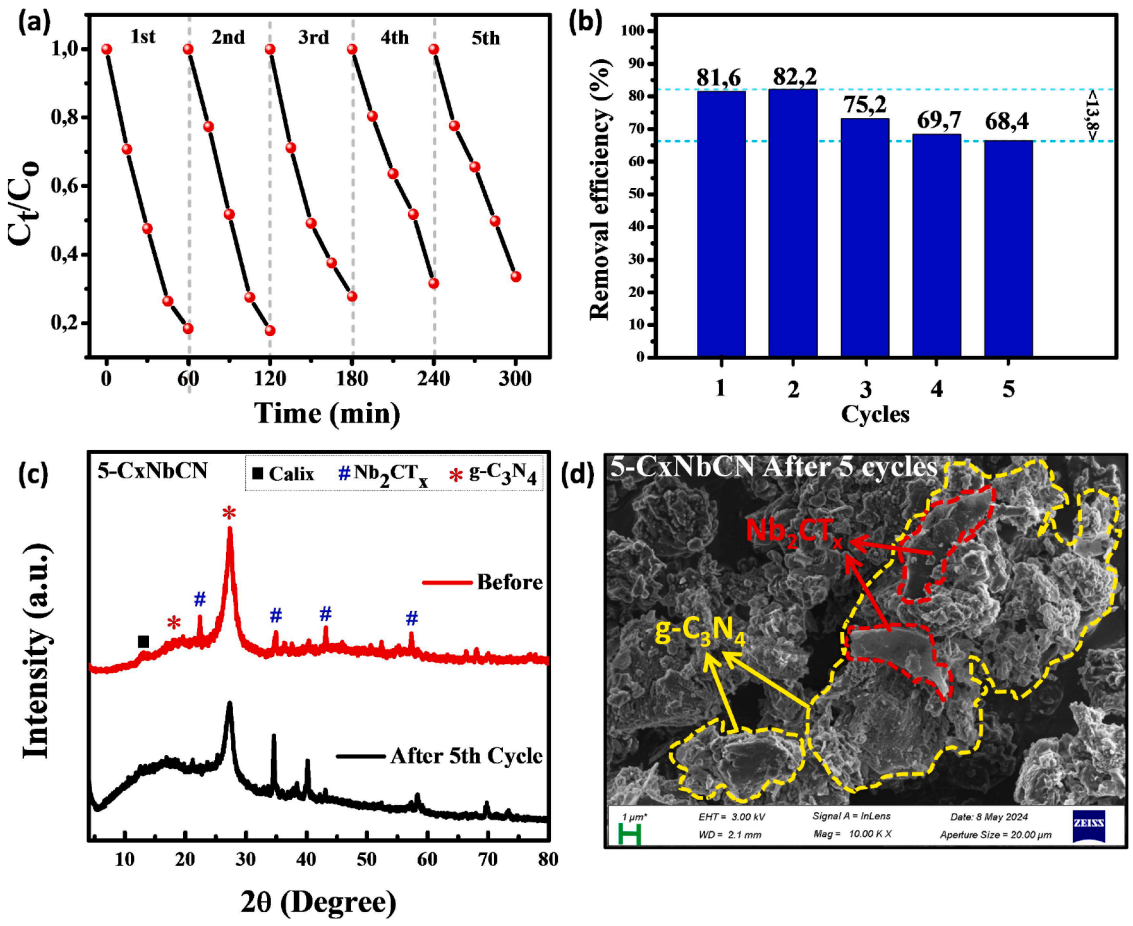


Fig. 14. Photodegradation recyclability studies for HCQ (a), comparative degradation efficiencies for HCQ (b), XRD spectra (c), and 5-CxNbCN SEM image (d) after five photodegradation cycles.

photodegradation intermediate products and the decomposition pathways for HCQ were derived using the mass spectra data depicted in **Fig. S7**. The mass chromatograph in **Fig. S7 (a)** was recorded for the parent HCQ complex prior to photodegradation, and **Fig. S7 (b-f)** were acquired after 120 min of irradiation in at different retention times. The corresponding HCQ plausible intermediate products of interests are presented as inserts in **Fig. S7**. The photodegradation of HCQ followed four pathways (P(A), P(B), P(C), and P(D)) derived from the chromatograph m/z data (Fig. 15). Initially, the parent hydroxychloroquine sulfate ($m/z = 433.14$) complex dissociated into cationic hydroxychloroquine complex ($m/z = 336.18$) in aqueous solution with pH 4. The continuation of decompositions proceeded from the cationic hydroxychloroquine complex as follows: intermediate product A (2-(ethyl(4-(quinolin-4-ylamino)pentyl)amino) ethanol, denoted IP(A)) was formed as a result of dehalogenation of Cl from hydroxychloroquine, followed by formation of IP(B) (quinoline, $m/z = 129.06$), IP(C) (4-(quinolin-4-ylamino)pentan-1-ylium, $m/z = 213.14$), IP (D) (N-ethyl-4-(quinolin-4-ylamino)pentan-1-aminium, $m/z = 258.20$), and IP(E) (quinolin-4-aminium, $m/z = 145.08$) through terminal organic chain fragmentations. Moreover, IP(F) (2-((4-((7-chloroquinolin-4-yl) amino)pentyl)(ethyl)amino)ethan-1-ylium, $m/z = 318.17$) resulted from dehydration of the hydroxychloroquine through pathway B. The fragment IP(I) (4-((7-chloroquinolin-4-yl)amino)-N-ethylpentan-1-aminium, $m/z = 292.16$) was formed through the 2-hydroxyethan-1-ide removal which assembled into a stable epoxide. Intermediate product IP(H) (7-chloro-N-ethylidenequinolin-4-aminium, $m/z = 205.05$) resulted from IP(I) through deamination of the secondary amine complex. Fragmentation of hydroxychloroquine through pathway D resulted in the formation of IP(G) (7-chloroquinolin-4-aminium, $m/z = 179.04$). Further decomposition of quinoline through oxaaldehyde removal resulted in the formation of IP(J) (2-aminobenzaldehyde, $m/z = 121.05$).

The LC-MS/MS data was also analysed for OS to evaluate the transformation intermediates resulting from the photodegradation processes. Mass spectrum for OS before light irradiation and after 120 min of irradiation at different retention times is presented in **Fig. S8**. The depicted mass spectra shows inserts with plausible intermediate species formed upon photodegradation of the parent OS complex using 5-CxNbCN under visible light irradiations (**Fig. S8**). Furthermore, The OS degradation pathways were proposed as shown in Fig. 16 and the intermediate products (IP) were numbered from IP1 to IP11. The OS degradation pathways can be summarised as follows: the initially dissolved oseltamivir phosphate (OSP, $m/z = 410.18$) in acidic aqueous solution dissociate into a cationic oseltamivir ($m/z = 313.21$), followed by the deamination of cationic amide through path (I) to form IP1 (6-acetamido-3-(ethoxycarbonyl)-5-(pentan-3-yloxy)cyclohex-3-en-1-ylium, $m/z = 296.19$), path (II) following caboxylesterase process to hydrolyse the ester functional group leading to the formation of IP2

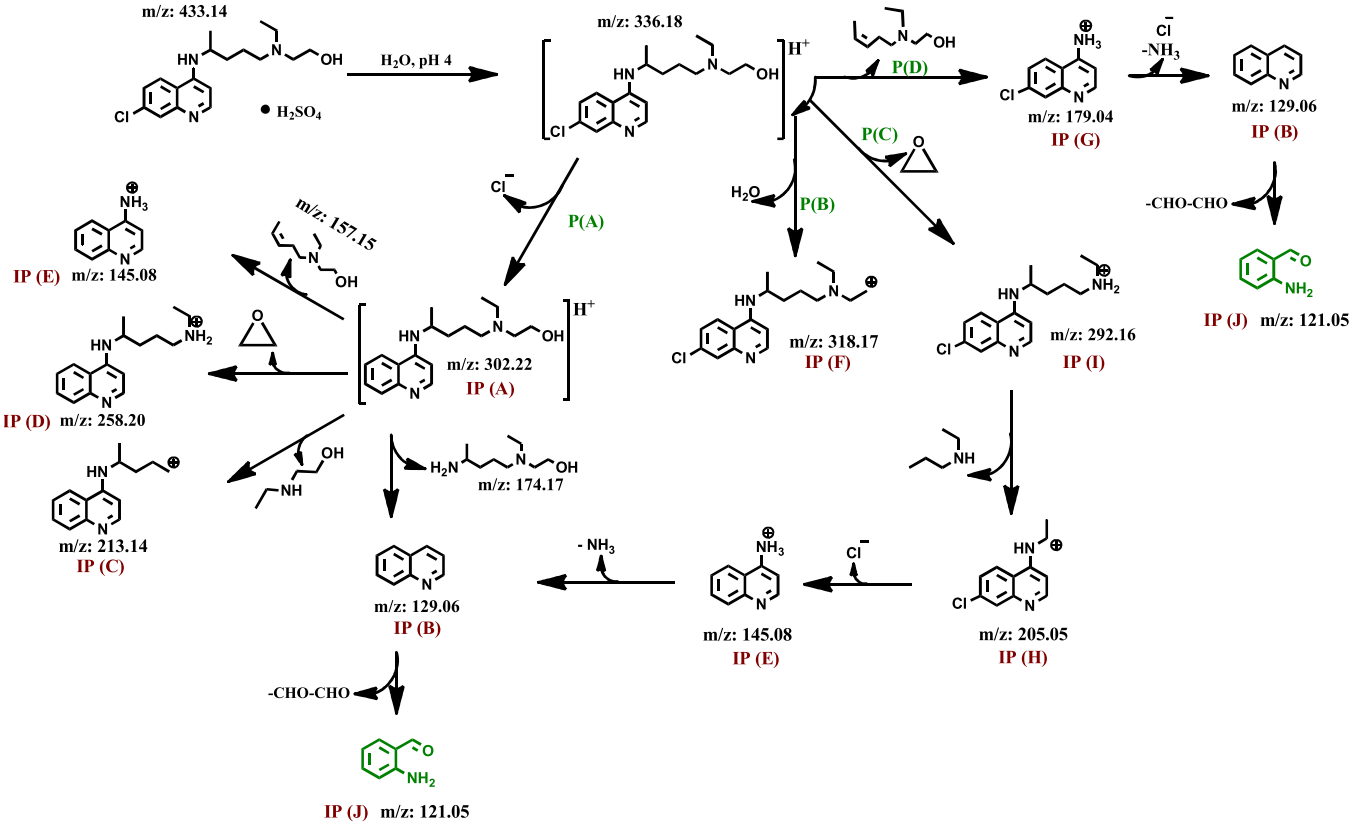


Fig. 15. Proposed photocatalytic degradation pathways of hydroxychloroquine sulphase (HCQ) using calixarene@Nb_2CT_x@g-C_3N_4 photocatalyst.

carboxylic acid complex (6-acetamido-3-carboxy-5-(pentan-3-yloxy) cyclohex-3-enaminium, m/z = 285.18), path (III) facilitated by hydration of alkene to alcohol to form IP3 (4-acetamido-5-amino-2-hydroxy-3-(pentan-3-yloxy)cyclohexanecarboxylic acid, m/z = 302.18), IP3 further fragmented into IP4 (4-acetamido-5-amino-2,3-dihydroxycyclohexanecarboxylic acid, m/z = 232.11) through hydroxyl radical (•OH) attack on the C_5H_{11} terminal group. Moreover, further fragmentation occurred through the proposed path (IV), where initial deamination of IP2 led to the formation of IP5 (6-acetamido-3-carboxy-5-(pentan-3-yloxy)cyclohex-3-en-1-ylium, m/z = 268.15), followed by formation of IP6 (m/z = 198.08), IP7 (m/z = 156.07), IP8/IP9 (m/z = 112.05/113.06), IP10 (m/z = 140.05), and IP11 (m/z = 95.05) through a sequence of removal of carbon chains, ketone, amine, carboxylic acid, and dehydration, correspondingly. The relatively smaller fragment IP11 (3-hydroxycyclohexa-2,5-dien-1-ylium, m/z = 95.05) was observed, which could fragment further into possible ammonium ions, H_2O, and CO_2 [54].

4. Conclusions

In summary, a hyphenated bio-photo degradation treatment system was successfully engineered and utilized for the removal of antiviral drugs hydroxychloroquine sulphate (HCQ) and oseltamivir phosphate (OS) from real wastewater. The operation of lab-scale wastewater treatment plant and the photocatalytic reactor were successfully optimized through a continuous acclimatization and sequential variation of operating parameters, respectively. Under optimal sludge operating conditions, the COD removal in the presence of HCQ and OS reached up to 56.1 and 45.5 % respectively. The 250 W visible light exhibited incident photon flux of I_o = 3.2 mEinstein.min^{-1} relative to the 2.4 mEinstein.min^{-1} of the UV light. The calixarene-sensitized Schottky-junction 5-Calixarene@Nb_2CT_x@g-C_3N_4 (5-CxNbCN) presented excellent photodegradation efficiency of up to 97.3 and 92.6 % for HCQ and OS in the hyphenated bio-photo degradation, correspondingly. The Langmuir-Hinshelwood pseudo-first-order kinetics were used to derive the reaction rate constants, where the degradation (bio-photo) presented rate constant of 3.23 × 10^{-2} and 2.51 × 10^{-2} min^{-1} for HCQ and OS using 5-CxNbCN under visible light irradiation, respectively. The composite 5-CxNbCN exhibited 2.6 times reaction rate constant relative to CN. The observed enhanced degradation efficiencies were attributed to the excellent optical and photoelectrochemical attributes possessed by the sensitized Schottky-junction. Additionally, the major contributors to ROS production toward the degradation of HCQ and OS were credited to the e^- and •O_2^-. The photocatalysts also exhibited good recyclability and stability over five degradation cycles, with an insignificant 13.8 % decrease for HCQ and 4.4 % for OS after the 5th cycles. The most plausible OS and HCQ photodegradation intermediate fragments and pathways were deduced from liquid chromatograph mass spectra data. The parent OS and HCQ ARVs decomposed into smaller organic molecules 3-hydroxycyclohexa-2,5-dien-1-ylium and 2-aminobenzaldehyde, respectively. The above findings provide an imperative scientific pathway for practical approach towards addressing global challenges

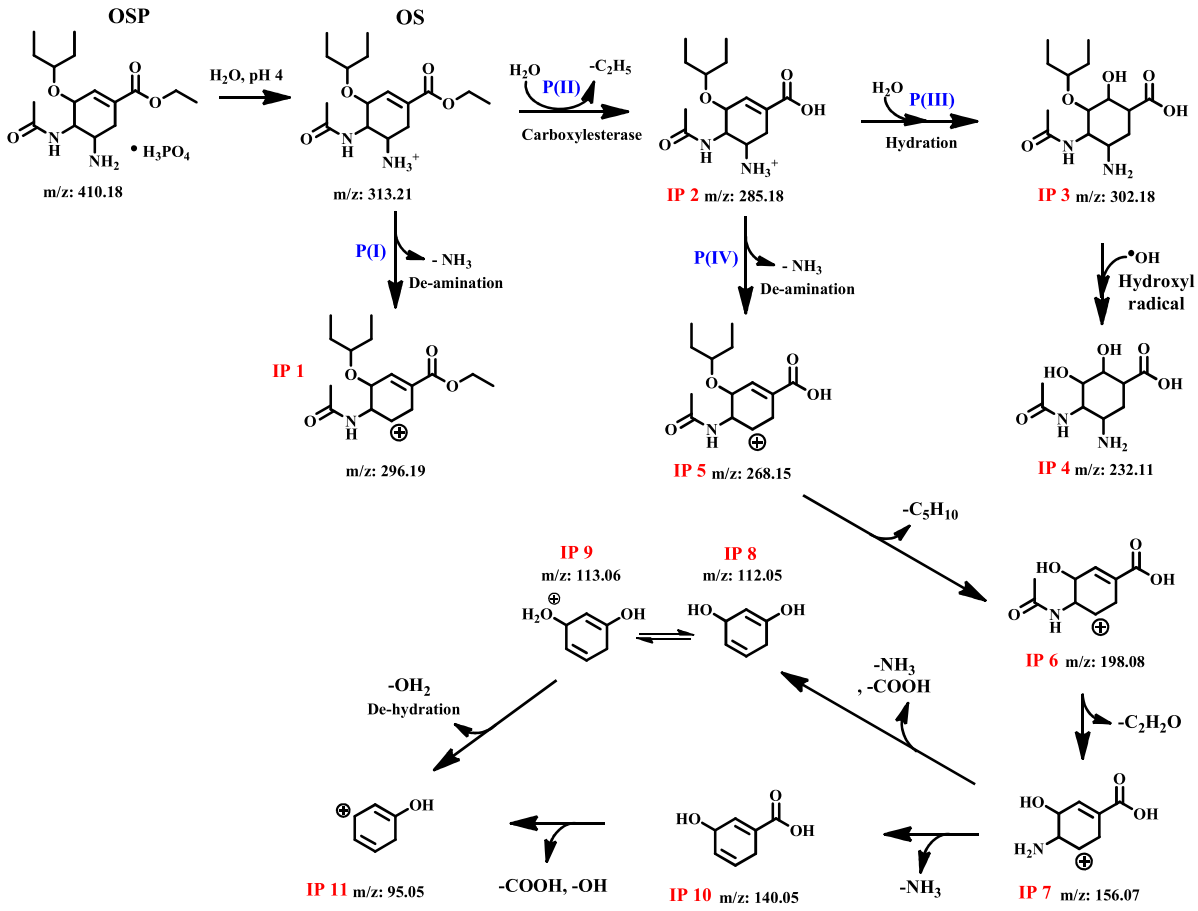


Fig. 16. Proposed photocatalytic degradation pathways of oseltamivir phosphate (OS) using calixarene@Nb_2CT_x@g-C_3N_4 (5-CxNbCN) photocatalyst.

faced due to the presence of pharmaceuticals in wastewater treatment systems.

Funding information

This work was funded by the University of Johannesburg (URC) and Faculty of Science (FRC), and the National Research Foundation (South Africa) - CSUR (SRUG210223587616). Student funding support from the National Research Foundation and the German Academic Exchange Service (NRF-DAAD).

CRediT authorship contribution statement

Lekgowa C. Makola: Writing – review & editing, Writing – original draft, Visualization, Methodology, Investigation, Formal analysis, Conceptualization. **Sharon Moeno:** Writing – review & editing, Validation, Supervision, Formal analysis, Data curation. **Langelihle N. Dlamini:** Writing – review & editing, Validation, Supervision, Methodology, Funding acquisition, Conceptualization.

Declaration of competing interest

The authors declare that they have no known competing financial interests or any personal relationships that could have appeared to influence the work reported in this paper.

Acknowledgements

The authors would like to acknowledge the University of Johannesburg (URC) and Faculty of Science (FRC), National Research Foundation - CSUR (SRUG210223587616), and National Research Foundation and the German Academic Exchange Service (NRF-DAAD) for research and study financial support. Authors would like to also acknowledge the much appreciated assistance with data acquisitions for liquid chromatography mass spectrometry and ultraviolet-visible spectrophotometer by Ntando Lele and Valentia Pheladi Letswalo, respectively.

Supplementary materials

Supplementary material associated with this article can be found, in the online version, at doi:10.1016/j.ceja.2025.100781.

Data availability

Data will be made available on request.

References

[1] J.K. Taubenberger, D.M. Morens, 1918 Influenza: the mother of all pandemics, Emerg. Infect. Dis. 12 (2006) 15–22.
[2] Y.C. Liu, R.L. Kuo, S.R. Shih, COVID-19: the first documented coronavirus pandemic in history, Biomed. J. 43 (2020) 328–333.
[3] https://www.worldometer.info/coronavirus: Webpage [Accessed 10-01-2024].
[4] T.-C. Ho, Y.-H. Wang, Y.-L. Chen, W.-C. Tsai, C.-H. Lee, K.-P. Chuang, Y-M.A. Chen, C.-H. Yuan, S.-Y. Ho, M.-H. Yang, Y.-C. Tyan, Chloroquine and hydroxychloroquine: efficacy in the treatment of the COVID-19, Pathogens. 10 (2021) 217.
[5] A. Zendehdel, M. Bidkhori, M. Ansari, S. Jamalimoghaddamsiyahkali, A. Asoodeh, Efficacy of oseltamivir in the treatment of patients infected with Covid-19, Ann. Med. Surg. 77 (2022) 103679.
[6] M. Kumar, K. Kuroda, K. Dhangar, P. Mazumder, C. Sonne, J. Rinklebe, M. Kitajima, Potential emergence of antiviral-resistant pandemic viruses via

environmental drug exposure of animal reservoirs, Environ. Sci. Technol. 54 (2020) 8503–8505.
[7] S. Horn, B. Vogt, R. Pieters, H. Bouwman, C. Bezuidenhout, Impact of potential COVID-19 treatment on South African water sources already threatened by pharmaceutical pollution, Environ. Toxicol. Chem. 39 (2020) 1305–1306.
[8] C. Swanepoel, H. Bouwman, R. Pieters, C. Bezuidenhout, Presence, Concentrations and Potential Implications of HIV-anti-retrovirals in Selected Water Resources in South Africa, Water Research Commission, Gezina, Pretoria, South Africa, 2015. https://wrcwebsite.azurewebsites.net/wp-content/uploads/mdocs/2144-1-14.pdf. Webpage [Accessed 13-01-2024].
[9] O.A. Abafe, J. Spath, J. Fick, S. Jansson, C. Buckley, A. Stark, B. Pietruschka, B. S. Martincigh, LC-MS/MS detection of antiretroviral drugs in influents and effluents from wastewater treatment plants in KwaZulu-Natal, South Africa, Chemosphere 200 (2018) 660.
[10] R.P. Nippes, P.D. Macruz, G.N. da Silva, M.H.N.O. Scaliante, A critical review on environmental presence of pharmaceutical drugs tested for the covid-19 treatment, Process Saf. Environ. Protect. 152 (2021) 568–582.
[11] X. Xu, Y. Huang, Construction of ternary CN/Ag/P25 photocatalysts for naphthalene photodegradation, Mater. Lett. 358 (2024) 135810.
[12] N. Lele, M.F. Bambo, E.M. Mmutlane, L.N. Dlamini, Construction of a multifunctional MXene@β-cyclodextrin nanocomposite with photocatalytic properties, Emergent. Mater. 6 (2023) 605–626.
[13] R. Sangamnere, T. Misra, H. Bherwani, A. Kapley, R. Kumar, A critical review of conventional and emerging wastewater treatment technologies, Sustain. Water. Resour. Manage 9 (2023) 58.
[14] https://www.nasa.gov/wp-content/uploads/2015/03/135642main_balance_trifold21.pdf: Webpage [Accessed 13-01-2024].
[15] B.M.F. Jones, G. Mamba, D. Maruthamani, V. Muthuraj, Honeycomb Nb_2O_5/RGO wrapped on MoO_3 nanorods for visible light-driven degradation of sulfasalazine and ciprofloxacin in water, Colloids Surfaces A: Physicochem. Eng. Aspects 653 (2022) 129836.
[16] V.P. Letswalo, L.N. Dlamini, S.P. Malinga, Efficient degradation of tetracycline using a nanostructured g-C_3N_4/Nb_2O_5/HPEI/PES photocatalytic membrane, Environ. Adv. 10 (2022) 100322.
[17] G. Kumar, I. Mukherjee, M. Dubey, B.P. Vellenki, R.K. Dutta, Photocatalytic degradation of tetracycline in aqueous medium using $ZnWO_4$/Bi_2MoO_6 nanocomposites under natural sunlight, Int. J. Environ. Sci. Technol. 20 (2023) 2903–2918.
[18] L. Wang, Q. Li, J. Song, X. Lu, Z. Tian, Y. Liu, J. Zhang, Construction of hierarchical $FeIn_2S_4$/BiOBr S-scheme heterojunction with enhanced visible-light photocatalytic performance for antibiotics degradation, Adv. Powder Technol. 33 (2022) 103859.
[19] I. Rapti, T. Kourkouta, E.-M. Malisova, T. Albanis, I. Konstantinou, Photocatalytic degradation of inherent pharmaceutical concentration levels in real hospital WWTP effluents using g-C_3N_4 catalyst on CPC Pilot scale reactor, Molecules. 28 (2023) 1170.
[20] Y.A. Bhembe, L.P. Lukhele, L. Hlekelele, S.S. Ray, A. Sharma, D-V.N. Vo, L. N. Dlamini, Photocatalytic degradation of nevirapine with a heterostructure of few-layer black phosphorus coupled with niobium (V) oxide nanoflowers (FL-BP@ Nb_2O_5), Chemosphere 261 (2020) 128159.
[21] E. Evgenidou, K. Vasilopoulou, E. Ioannidou, L.A. Koronaiou, C. Nannou, D. G. Trikkaliotis, D. Bikiaris, G.Z. Kyzas, D. Lambropoulou, Photocatalytic degradation of the antiviral drug abacavir using titania-graphene oxide nanocomposites in landfill leachate, J. Photochem. Photobiol. 439 (2023) 114628. A: Chemistry.
[22] P.V. Gayathri, D. Nair, G. Gopinath, D. Pilla, S. Joseph, Solar photocatalysis for the decontamination of water from emerging pharmaceutical pollutant chloroquine using nano ZnO as the catalyst, Water. Air. Soil. Pollut. 234 (2023) 146.
[23] OECD, Test No. 303: Simulation Test - Aerobic Sewage Treatment A: Activated Sludge Units; B: Biofilms, OECD Guidelines for the Testing of Chemicals, Section 3, OECD Publishing, Paris, 2001, pp. 1–50, https://doi.org/10.1787/9789264070424-en [Accessed 24-01-2024].
[24] L.C. Mahlalela, C. Casado, J. Marugan, S. Septien, T. Ndlovu, L.N. Dlamini, Coupling biological and photocatalytic treatment of atrazine and tebuthiuron in aqueous solution, J. Water. Process. Eng. 40 (2021) 101918.
[25] M.L. Malati, L.C. Mahlalela, S.P. Malinga, L.N. Dlamini, Impact of macromolecules on the stability of MoS_2 nanosheets and understanding the fate and behavior simulated in a wastewater treatment plant under aerobic conditions, Int. J. Environ. Res. 16 (2022) 44.
[26] Water Environment Federation, Process Control for Activated Sludge, 2013, in: https://www.wefnet.org/ProcessCtrlActivatedSludge/Process%20Control%20for%20Activated%20Sludge_Color.pdf. Webpage [Accessed 20-01-2024].
[27] American Water Chemicals, Activated Sludge Process. https://www.membranechemicals.com/water-treatment/activated-sludge-process/Webpage [Accessed 20-01-2024].
[28] Q. Xu, P. Wang, Z. Wang, J. Shen, X. Han, X. Zheng, Y. Wei, C. Li, K. Song, Aerosol self-assembly synthesis of g-C_3N_4/MXene/Ag_3PO_4 heterostructure for enhanced photocatalytic degradation of tetracycline hydrochloride, Colloids Surfaces A: Physicochem. Eng. Aspects 648 (2022) 129392.
[29] N. Liu, N. Lu, H. Yu, S. Chen, X. Quan, Efficient day-night photocatalysis performance of 2D/2D Ti_3C_2/porous g-C_3N_4 nanolayers composite and its application in the degradation of organic pollutants, Chemosphere 246 (2020) 125760.
[30] D. Zhu, Q. Zhou, Action and mechanism of semiconductor photocatalysis on degradation of organic pollutants in water treatment: a review, Environ. Nanotechnol. Monit. Manage 12 (2019) 100255.
[31] L.C. Makola, S. Moeno, C.N.M. Ouma, A. Sharma, D.V.N. Vo, L.N. Dlamini, Facile fabrication of a metal-free 2D-2D Nb_2CT_x@g-C_3N_4 MXene-based Schottky-heterojunction with the potential application in photocatalytic processes, J. Alloys. Compd. 916 (2022) 165459.
[32] L.C. Makola, C.N.M. Ouma, S. Moeno, E.M. Mmutlane, L.N. Dlamini, An insight into a novel calixarene-sensitized Calix@Nb_2CT_x/g-C_3N_4 MXene-based photocatalytic heterostructure: fabrication, physicochemical, optoelectronic, and photoelectrochemical properties, J. Sci.: Adv. Mater. Devices 8 (2023) 100593.
[33] S. Simelane, J.S. Ngila, L.N. Dlamini, The fate, behaviour and effect of WO_3 nanoparticles on the functionality of an aerobic treatment unit, Environ. Nanotechnol. Monit. Manage 8 (2017) 199–208.
[34] X. Zhuang, X. Li, Y. Yang, N. Wang, Y. Shang, Z. Zhou, J. Li, H. Wang, Enhanced sulfamerazine removal via adsorption-photocatalysis using Bi_2O_3-TiO_2/PAC ternary nanoparticles, Water. (Basel) 12 (2020) 2273.
[35] G.C. Hatchard, C.A. Parker, A new sensitive chemical actinometer II. Potasium ferrioxalate as a standard chemical actinometer, Proc. R. Soc. A 235 (1956) 518–536.
[36] D.T. Ruziwa, A.E. Oluwalana, M. Mupa, L. Meili, R. Selvasembian, M.M. Nindi, M. Sillanpaa, W. Gwenzi, N. Chaukura, Pharmaceuticals in wastewater and their photocatalytic degradation using nano-enabled photocatalysts, J. Water. Process. Eng. 54 (2023) 103880.
[37] S. Sharma, A.O. Ibhadon, M.G. Francesconi, S.K. Mehta, S. Elumalai, S.K. Kansal, A. Umar, S. Baskoutas, Bi_2WO_6/C-dots/TiO_2: a novel Z-scheme photocatalyst for the degradation of fluoroquinolone levofloxacin from aqueous medium, Nanomaterials 10 (2020) 910.
[38] M.L. Malati, A. Abrahams, V. Chauke, M.P. Seopela, L.N. Dlamini, Monitoring and optimizing the biocatalytic degradation of efavirenz with immobilized Trametes versicolor laccase on Ti2NTx MXene: a lab-scale wastewater treatment plant process, J. Environ. Chem. Eng. 11 (2023) 110420.
[39] L. Cheng, Q. Chen, J. Li, H. Liu, Boosting the photocatalytic activity of $CdLa_2S_4$ for hydrogen production using Ti_3C_2 MXene as a co-catalyst, Appl. Catal. B: Environ. 267 (2020) 118379.
[40] S. Li, C. Wang, Y. Liu, M. Cai, Y. Wang, H. Zhang, Y. Guo, W. Zhao, Z. Wang, X. Chen, Photocatalytic degradation of tetracycline antibiotic by a novel $Bi_2Sn_2O_7$/Bi_2MoO_6 S-scheme heterojunction: performance, mechanism insight and toxicity assessment, Chem. Eng. J. 429 (2022) 132519.
[41] P. Pal, Biological treatment technology, in: P. Pal (Ed.), Industrial Water Treatment Process Technology, Butterworth-Heinemann, 2017, pp. 65–144, https://doi.org/10.1016/B978-0-12-810391-3.00003-5.
[42] Z. Jiang, Z. Xia, S. Liu, Q. Wei, H. Fan, L. Qi, G. Liu, H. Wang, The effect of fine grits and fine debris concentrations on the MLVSS/MLSS ratio of an activated sludge system, J. Environ. Sci. 147 (2025) 607–616.
[43] P. Wongburi, J.K. Park, Prediction of sludge volume index in aWastewater treatment plant using recurrent neural network, Sustainability. 14 (2022) 6276.
[44] L.C. Mahlalela, C. Casado, J. Marugan, S. Septien, T. Ndlovu, L.N. Dlamini, Photocatalytic degradation of atrazine in aqueous solution using hyperbranched polyethyleneimine templated morphologies of $BiVO_4$ fused with Bi_2O_3, J. Environ. Chem. Eng. 8 (2020) 104215.
[45] A.L. Onungwu, C.S. Nwagwu, O.S. Onugwu, A.C. Echezona, C.P. Agbo, S.A. Ihim, P. Emeh, P.O. Nnamani, A.A. Attama, V.V. Khutoryanskiy, Nanotechnology based drug delivery systems for the treatment of anterior segment eye diseases, J. Control. Rel. 354 (2023) 465–488.
[46] L.C. Mahlalela, J.C. Ngila, L.N. Dlamini, Characterization and stablillity of TiO_2 nanoparticles in industrial dye stuff effluent, J. Dispers. Sci. Technol. 38 (2017) 584–593.
[47] M. Zielinska, I. Wojnowska-baryla, A. Cydzik-kwiatkowska, Bisphenol A Removal from Water and Wastewater, Springer Nature, Gewerbestrasse, Switzerland, 2019, pp. 29–36.
[48] R.L. Schroeder, J.P. Gerber, Chloroquine and hydroxychloroquine binding to melanin: some possible consequences for pathologies, Toxicol. Rep. 1 (2014) 963–968.
[49] M.D. Green, H. Nettey, R.A. Wirtz, Determination of Oseltamivir quality by colorimetric and liquid chromatographic methods, Emerg. Infect. Dis. 14 (2008) 552–556.
[50] J. Zhang, H. Wu, L. Shi, Z. Wu, S. Zhang, S. Wang a, H. Sun, Photocatalysis coupling with membrane technology for sustainable and continuous purification of wastewater, Sep. Purif. Technol. 329 (2024) 125225.
[51] Z.H. Jabbar, A.A. Okab, B.H. Graimed, S.H. Ammar, H. Taofeeq, M. Al-Yasiri, Building a robust S-scheme BiOCl/$CuBi_2O_4$ system for photocatalytic oxidation of sulfamethoxazole under solar light irradiation, Solar Energy 275 (2024) 112640.
[52] X. Jia, F. Wang, X. Xu, C. Liu, L. Zhang, S. Jiao, G. Zhu, X. Wang, G. Yu, Highly efficient photocatalytic degradation of tetracycline by modifying UiO-66 via different regulation strategies, ACS. Omega 8 (2023) 27375–27385.
[53] Chao-Ping Hou, Xin-Ao Li, Jian-Feng Huang, Jun-Min Liu, Hydrophilic calix[4] arene dye-sensitized Co/g-C_3N_4 composites with Co single atoms for enhanced visible-light-driven photocatalysis, Dyes Pigments 220 (2023) 111728.
[54] M.E. Malefane, M. Managa, T.T.I. Nkambule, A.T. Kuvarega, S-scheme 3D/3D Bi/BiOBr/P doped g-C_3N_4 with oxygen vacancies (Ov) for photodegradation of pharamceuticals: in-situ H_2O_2 production and plasmon induced stability, ChemSusChem. (2024) e202401471.
[55] X. Yi, J. Yuan, H. Tang, Y. Du, B. Hassan, K. Yin, Y. Chen, X. Liu, Embedding few-layer $Ti_3C_2T_x$ into alkalized g-C_3N_4 nanosheets for efficient photocatalytic degradation, J. Colloid. Interface Sci. 571 (2020) 297–306.
[56] N. Liu, N. Lu, Y. Su, P. Wang, X. Quan, Fabrication of g-C_3N_4/Ti_3C_2 composite and its visible-light photocatalytic capability for ciprofloxacin degradation, Sep. Purif. Technol. 211 (2019) 782–789.

[57] H. Zhang, J. Xu, Y. Yuan, Y. Guo, X. Tan, H. Wang, X. Hu, C. Tang, Highly conductive Ti_3C_2 MXene reinforced g-C_3N_4 heterojunction photocatalytic for the degradation of ciprofloxacin: mechanism insight, Sep. Purif. Technol. 330 (2024) 125520.

[58] W.-L. Wang, Q.-Y. Wu, Z.-M. Wang, H.-Y. Hu, N. Negishi, M. Torimura, Photocatalytic degradation of the antiviral drug Tamiflu by UV-A/TiO_2: kinetics and mechanisms, Chemosphere 131 (2015) 41–47.

[59] B. Saini, G. Bansal, Characterization of four new photodegradation products of hydroxychloroquine through LC-PDA, ESI-MSn and LC-MS-TOF studies, J. Pharm. Biomed. Anal. 84 (2013) 224–231.